International Journal of Engineering Research & Innovation

Editor-in-Chief: Mark Rajai, Ph.D.
California State University Northridge
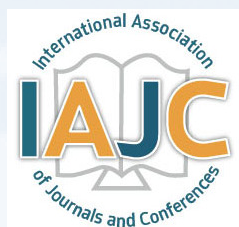
INTERNATIONAL JOURNAL OF ENGINEERING RESEARCH AND INNOVATION

ABOUT IJERI:

- IJERI is the second official journal of the International Association of Journals and Conferences (IAJC).

- IJERI is a high-quality, independent journal steered by a distinguished board of directors and supported by an international review board representing many well-known universities, colleges, and corporations in the U.S. and abroad.

- IJERI has an impact factor of **1.58**, placing it among an elite group of most-cited engineering journals worldwide.

OTHER IAJC JOURNALS:

- The International Journal of Modern Engineering (IJME) For more information visit www.ijme.us

- The Technology Interface International Journal (TIIJ) For more information visit www.tiij.org

IJERI SUBMISSIONS:

- Manuscripts should be sent electronically to the manuscript editor, Dr. Philip Weinsier, at philipw@bgsu.edu.

  For submission guidelines visit www.ijeri.org/submissions

TO JOIN THE REVIEW BOARD:

- Contact the chair of the International Review Board, Dr. Philip Weinsier, at philipw@bgsu.edu.

  For more information visit www.ijeri.org/editorial

INDEXING ORGANIZATIONS:

- IJERI is indexed by numerous agencies. For a complete listing, please visit us at www.ijeri.org.
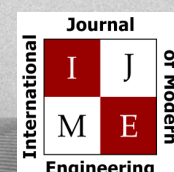
Contact us:

Mark Rajai, Ph.D.

Editor-in-Chief
California State University-Northridge
College of Engineering and Computer Science
Room: JD 4510
Northridge, CA 91330
Office: (818) 677-5003
Email: mrajai@csun.edu

www.tiij.org

www.ijme.us

INTERNATIONAL JOURNAL OF ENGINEERING RESEARCH AND INNOVATION

THE INTERNATIONAL JOURNAL OF ENGINEERING RESEARCH AND INNOVATION EDITORS

TABLE OF CONTENTS

5th IAJC/ISAM Joint International Conference
November 6 – 8, 2016, Orlando, Florida

The leading indexed high impact factor conference
on engineering and related technologies.
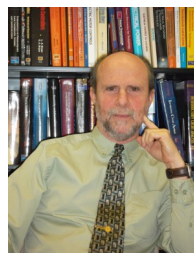
EDITOR'S NOTE

Philip Weinsier, IJERI Manuscript Editor

The editors and staff at IAJC would like to thank you, our readers, for your continued support, and we look forward to seeing you at the upcoming IAJC conference. For this fifth IAJC conference, we will again be partnering with the International Society of Agile Manufacturing (ISAM). This event will be held at the new Embassy Suites hotel in Orlando, FL, November 6-8, 2016. The IAJC/ISAM Executive Board is pleased to invite faculty, students, researchers, engineers, and practitioners to present their latest accomplishments and innovations in all areas of engineering, engineering technology, math, science, and related technologies.

In additional to our strong institutional sponsorship, we are excited this year to announce that nine (9) high impact factor (IF) ISI journals asked to sponsor our conference as well, and wish to publish some of your best papers. But I would be remiss if I didn't take this opportunity to remind you of the excellent impact factors (Google Scholar method) for our own three journals. The International Journal of Modern Engineering (IJME) has a remarkable IF = 3.00. The International Journal of Engineering Research and Innovation (IJERI) has an IF = 1.58, which is noteworthy, as it is a relatively young journal, only in publication since 2009. And the Technology Interface International Journal (TIIJ) with an IF = 1.025. Any IF above 1.0 is considered high, based on the requirements of many top universities, and places the journals among an elite group.

Selected papers from the conference will be published in the three IAJC-owned journals and possibly the nine ISI journals. Oftentimes, these papers, along with manuscripts submitted at-large, are reviewed and published in less than half the time of other journals. Publishing guidelines are available at www.iajc.org, where you can read any of our previously published journal issues, as well as obtain information on chapters, membership, and benefits.

> Main Sponsors

Editorial Review Board Members

Development of a Passive Radio Frequency Identification-Based Sensor for External Corrosion Detection

Yizhi Hong, Texas A&M University; Pranav Kannan, Texas A&M University; Brian Z. Harding, Texas A&M University; Hao Chen, Texas A&M University; Samina Rahmani, Texas A&M University; Ben Zoghi, Texas A&M University; M. Sam Mannan, Texas A&M University

Abstract

Pipeline corrosion causes many incidents every year resulting in fatalities, injuries, and millions of dollars' worth of property damage. In order to maintain pipeline integrity and reduce the risk of having substantial pipeline incidents, a novel type of smart corrosion tag was developed by the authors in this current study. By using radio frequency identification (RFID) technology, the smart corrosion tag is able to provide continuous, real-time wireless monitoring of external pipeline corrosion. The effectiveness of the tags was verified in a custom-made environmental chamber with temperature, humidity, flow control, and electronic control. An on/off tag design was selected for its potential use in early detection of external pipeline corrosion, corrosion resistant coating failure, or indication of a corrosive environment. The corrosion rates of metal samples in soils with different pH levels were tested in order to provide a reference of the corrosion rate of the antenna of the RFID tag.

Introduction

Corrosion is a major problem across industries with annual direct costs of approximately $1.8 trillion [1]. A corrosion study conducted by the U.S. Federal Highway Administration states that the direct corrosion cost is equivalent to 3.1% of the nation's gross domestic product (GDP) from 1999 to 2001 [2]. It is also one of the leading causes of pipeline failures in the chemical, oil, and gas industries. A current statistic on significant pipeline incidents from the Pipeline and Hazardous Materials Safety Administration (PHMSA) shows that from 1995 to 2014, there were 1096 significant incidents involving pipeline corrosion [3]. Internal corrosion, external corrosion, and stress corrosion cracking are the three major types of corrosion failures in pipelines. About half of the incidents are caused by external pipeline corrosion, which occurs due to the interaction between the environment and the exterior of the pipeline.

Pipeline corrosion will inevitably occur; therefore, proper management is crucial in order to control and mitigate problems that stem from corrosion. Experience shows that pipelines can continue safely serving the needs of industry for decades, provided they are properly designed, inspected, and maintained [4]. According to the American Society of Mechanical Engineers (ASME) B31, Standards of Pressure Piping, a pipeline integrity management system is a mandatory process for assessing and mitigating pipeline risks [5, 6]. A strong corrosion management system starts with effective inspection, including effective corrosion monitoring and detection.

The most commonly used pipeline inspection methods include pigging, hydro-testing, external corrosion direct assessment (ECDA), and internal corrosion direct assessment (ICDA) [7-12]. However, there are downsides for existing inspection techniques. Most of the testing approaches, such as pigging and hydro-testing, are very expensive and can only be conducted periodically, providing only a snapshot of the corrosion situation. Direct excavation of the pipeline to examine its condition can be very expensive and time consuming, and may cause secondary damage to coatings. The sensitivity of pipe-to-soil potential testing is relatively low, and the potential value is dependent on the resistivity and moisture content of the soil. Other recent research on external detection methods involved electrochemical testing equipment, which increases the cost of inspection, thereby making practical applications difficult [13-18].

Corrosion can occur in a multitude of conditions, greatly complicating the detection and monitoring process. A novel type of smart corrosion tag using RFID technology was developed in this study that showed superior advantages.

This tag is
a) a continuous, real-time monitoring wireless non-contact system that streams constant signals regarding its current corrosion status from which appropriate maintenance decisions can be made.
b) inexpensive, expendable, and simple to deploy without interfering with existing onsite activities.
c) able to be monitored onsite on a regular basis with simple equipment and training.
d) universal and deployable in all ranges of conditions, including environmental conditions, operating conditions, geometries, locations, and materials.

RFID is a wireless sensor that detects electromagnetic signals. Two of the main advantages are that it can detect and store data in real-time and that it does not require human involvement [19, 20]. Typically, RFID systems include three components: an antenna, a transceiver, and a transponder with a unique identifier. The RF signal can be transmitted wirelessly over large distances through obstacles, thus providing the penetrating capability required for non-contact detection of corrosion.

RFID smart tags are either active, semi-active, or passive [21]. The smart RFID tags in this study were passive tags, which were not equipped with an internal energy source (such as batteries). Thus, it is a simple solution for continuous corrosion monitoring. As illustrated in Figure 1, the smart RFID tags can emit signals to detect the existence of pipeline corrosion by placing the RFID tags close to monitored locations on demand. The black wave represents the incoming radio wave from the reader. Under normal operating conditions, the RFID tag antenna receives the signal and powers the microchip. The microchip at a normal site then responds with a normal radio frequency signal (blue color waves in Figure 1). If the tag becomes corroded, the antenna can still receive the signal; however, the connection between the antenna and the microchip will be severed, preventing the microchip from receiving power and, therefore, responding, thus creating an on/off design. The change in responding signal allows corroded sites to be detected. The continuous signals from the RFID tags are then monitored and used as corrosion indicators.
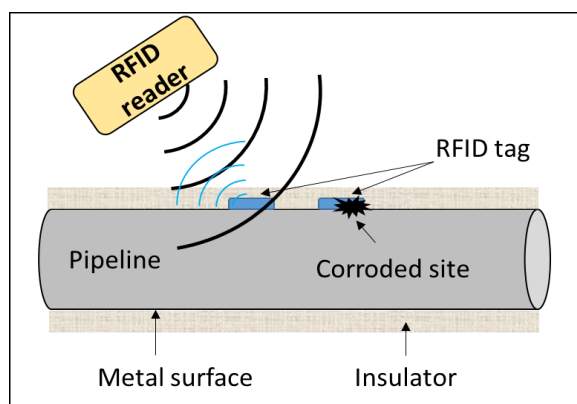
Figure 1. Conceptual Representation of Using Integrated RFID Corrosion Tag for Corrosion Monitoring under Insulation

Because radio frequency (RF) signals cannot penetrate metal, the application of RFID tags focuses on external pipeline corrosion detection in various conditions, such as underground and under insulation. They can also be used as an indication of a corrosive environment. External corrosion, high moisture content, poor drainage, and high salt and oxygen content of the soil tend to increase corrosivity [22, 23]. Thus, the tags provide an indication of the corrosivity of the soil, which is a leading indicator of coating failure.

Materer and Apblett [24] used RFID as a corrosion indicator with a tag design that used low-frequency RF. Although, this provided a novel solution for corrosion detection, it also had some limitations, due to the fragile design of the tag and the fact that low-frequency RF has a very short effective range. The tag designed in this study provides three factors that increase its effectiveness in real-world pipeline corrosion detection. The first is the use of ultra-high-frequency (UHF) RF, which increases the effective range up to 20 meters, making it much more applicable for buried pipelines. The second is a more robust tag design that cannot be severed by ground movement, causing a false corrosion indication. The third is the adjustable antenna thickness, which allows multiple tags of different thicknesses to be employed in the same environment, providing a multiple-point sample of soil corrosivity with less margin for error.

Material and Methods

RFID Tag Information

The RFID tags used in this study were passive UHF tags that follow the RF specification electronic product code (EPC) Gen 2/ISO 18000-6c standard with 96- or 512-bit memory and operate in the upper band (860-960 MHz). The tags were manufactured with the Alien Higgs 3 Standard Gen 2 UHF chip and Lincoln Electric SuperArc L-56 wires. When compared to other frequency bands that are typically used in RFID applications, such as 13.56 MHz and 125-150 kHz, UHF tags have superior distance performance in harsh environments with a higher data transfer rate, which is favorable for practical applications. Moreover, these RFID tags are very robust, designed for heavy duty tasks, and are easily attachable to the host objects by various methods such as adhesive, tape, Velcro strap, or zip-tie.

Two types of RFID smart tags were designed and tested in this study. Figures 2(a) and 2(b) show the schematic design and the physical picture of a pristine RFID tag. The chip is not protected, and the antenna is made of tightly twisted metal wires. Figures 2(c) and 2(d) show the schematic design and the physical picture of an on/off RFID smart tag. There is a corrosion-resistant plastic coating (HIX Polyolefin) covering both the chip and a majority of the antenna, with the exception of a small section of exposed antenna adjacent to the chip (the exposed section is approximately 1 cm long). In both tag designs, the total length of the tag is 17 cm and the chip is about 1 cm. The materials of

the antenna are alloys that are used in pipeline construction and, hence, the corrosion rate of the antenna is representative of the corrosion rate of the pipeline. However, other types of materials can also be employed.
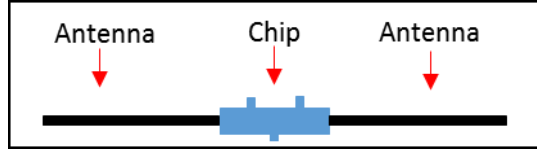
(a) Schematic Design of a Pristine RFID Tag

(b) A Pristine RFID Tag
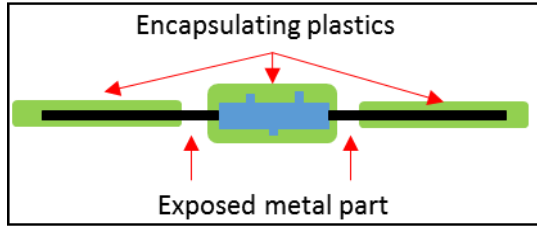
(c) Schematic Design of an On/Off RFID Tag
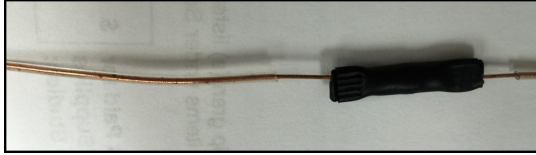
(d) An On/Off RFID Tag

Figure 2. Schematic and Picture of RFID Smart Tag Design

UHF passive RFID tags operate on the convention of transferring power between the reader and the tag. The first half of the communication between reader and tag is executed by the radiation of radio waves from the reader to the tag's integrated circuit. The other half is the backscatter tag to the reader, which is measured by a quantity known as the received signal strength indicator (RSSI), also referred to as the backscatter power of the tag. In free space, the power received by the reader can be expressed by Equation (1) [25, 26]:

$$P_{RSSI} = P_t \left[G_t g_r \left(\frac{\lambda}{4\pi d} \right)^2 \right] \left[G_r g_t \left(\frac{\lambda}{4\pi d} \right)^2 \right] \Gamma \qquad (1)$$

where, P_t is the power transmitted by the reader; P_{RSSI} is the power received by the reader antenna; G_t, g_t, and G_r, g_r are the gains of the reader and tag transmit and receive antennas, respectively; Γ is a reflection coefficient of the tag; λ is

the wavelength of the reader signal; and, d is the distance from the reader.

It was assumed that a more highly corroded tag would require a higher transmitted power in order to power on the tag, and that consequently the tag's RSSI would be diminished as well.

Environmental Chamber

A corrosion environment chamber was designed and constructed, which consisted of a chamber, temperature and humidity sensors (Vernier stainless steel temperature probe sensor and Vernier relative humidity sensor), UHF RFID reader/antenna (Impinj Speedway Revolution R420 RFID reader), a data acquisition board (Vernier SensorDAQ), and a custom-designed graphical user interface (GUI) software package. Figure 3 shows the schematic of the environmental chamber and a picture of the chamber. The chamber meets American Standard for Test and Measurement (ASTM) B117 standards. The Speedway UHF RFID reader is connected to a single antenna with power output between +10 and +30 dBm. The dimensions of the chamber are 31 cm × 76 cm × 48 cm (L×W×H). The reader uses a frequency-hopping modulation, as defined by Federal Communications Commission (FCC) *part 15.247* rules on digital modulation [27]. The hopping range for this device is the 902 – 928 MHz band.

As Figure 3(b) shows, there are six locations from 1 to 6 in the sample stage and a maximum of six RFID tags can be monitored in each experiment. The vertical distance from the reader to the sample stage is 66 cm. The GUI was designed based on LabVIEW virtual instrument (VI) programming for continuous temperature and humidity control and data acquisition.

Experimental Setup

The RFID tag experiments consisted of three parts: characterization testing, corrosion simulation testing, and corrosion testing. In order to use the RFID tag to monitor corrosion, a correlation between the corrosion conditions of the RFID tag antenna and the tag signal was required. First, the impact of major environmental conditions (i.e., temperature, humidity, position, and location characteristics) on tag signal were tested during the characterization testing in order to understand the feasibility of the RFID corrosion monitoring system. The next objective was to correlate RFID tag antenna corrosion with tag signal. In the preliminary stage, the simulation of RFID tag corrosion was accomplished by manually cutting the antenna. This corrosion simulation process allowed for quantification of the effects of physical

changes of the tag on RSSI and tuning frequency. During corrosion simulation testing, the RFID tags were placed in an acidic environment to test the effectiveness of corrosion monitoring. The corrosion test of RFID tags in an acid solution was accomplished by immersing the antenna parts in the acid solution, while keeping the chip exposed in the air. The realistic corrosion testing of the RFID tags was accomplished by directly embedding the tags in acidified soil. Table 1 shows all six experimental variables.
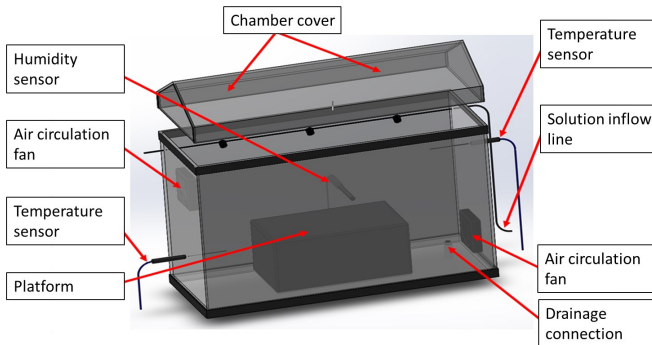
(a)   Schematic of the Environmental Chamber
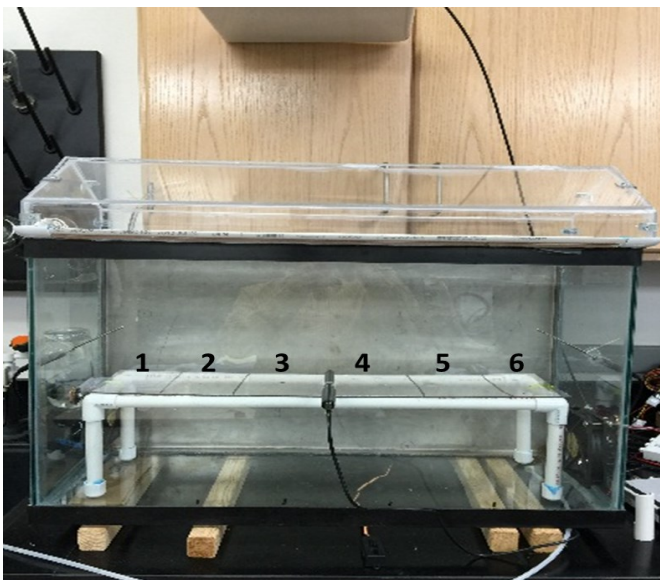
(b) Environmental Chamber with Tag Locations Marked

Figure 3. Front View of Chamber Design and Real Environmental Chamber

For each test, a similar protocol was used. Six RFID tags were placed on the sample stage inside the environmental chamber, as shown in Figure 3(b). The time of each experiment set was two hours, resulting in around 1400 RSSI data points for each RFID tag. The RSSI was analyzed by taking the mean, the standard deviation, and the range of the data.

Table 1. Experimental Variables of RFID Tag Testing

RFID testing	Variable	Descriptions
Characterization tests	Temperature	20 ^{0}C, 25 ^{0}C, 30 ^{0}C, 35 ^{0}C
	Humidity	30 %, 60 %, 100 %
	Reader-tag Distance	50 cm, 66 cm
Corrosion simulation testing	Length of tag (Pristine RFID tag)	17 cm, 16 cm (cut from one side), 15 cm (cut from two sides),…1 cm (cut from two sides)
	Length of tag (on/off RFID tag)	17 cm, 10 cm (cut from one side), 3 cm (cut from both sides)
Corrosion testing	Acid	H_2O, H_2SO_4 Solutions (1.25%, 2.5% and 5%), and acidified soil

After the experiments with the RFID tags, the corrosion rate measurements of commercial metal coupons in both acid solution and acidified soil were conducted to understand the pattern of corrosion and give a reference for the corrosion rate of the antenna of the RFID tag. The corrosion rate measurements were performed using gravimetric weight loss measurements.

The corrosion coupons, made from G1020 alloy (steel alloy, ½" x 3" x 1/16", glass bead finish), were procured from Metal Samples Inc. Before the experiments, the exposed surface of the metal coupon was mechanically abraded with 150- and 100-grain sandpapers, and then washed with Millipore (Milli-Q) water, degreased, and dried. Acid solutions with concentrations of 1.25%, 2.5%, and 5% were prepared by mixing sulfuric acid (ACS grade BDH catalog number – BDH3072) with Millipore water. The soil used in the tests was obtained from the areas surrounding the campus buildings (Jack E Brown Engineering Building, Texas A&M University). The coupons were buried in the acidified soil (200 cm^3 of soil mixed with 40 ml of dilute sulfuric acid) and sealed. There were six time points measured at three concentrations, as illustrated in Table 2. After the experiment, oxidation deposits on the surface of the metal coupon were removed by carefully sanding the surface with 150-grit sandpaper before drying and weighing.

Results

RFID Experiments

Because the RFID reader implements FCC mandated frequency hopping in the 902-928 MHz band, there were slight variations in the RSSI. Figure 4 shows a typical RSSI in the

experiment. In this experiment, the mean, standard deviation, and range of the data were recorded. The standard deviation of the signal fluctuated across different individual RFID tags (in a range of ±4 dB).

Table 2. Acid Concentration Added to Soil and Time Points

Acid concentration added to soil (Set I)	10%	5%	2.5%
Time points for Set I (Hours)	144	360	504
Acid concentration added to soil (Set II)	1.25%	0.5%	0.25%
Time points for Set II (Hours)	264	456	672
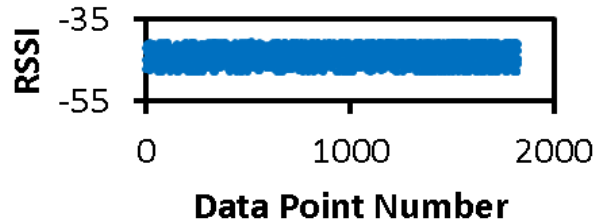
Figure 4. RFID Tag RSSI Signal Response

Figure 5 shows the effects of temperature and humidity on RSSI for the on/off RFID tag design. Temperature in the range of 20-35°C had no significant effect on the reading, and humidity in the range of 30%-100% had only a minor influence on the signal reading, considering the inherent variance of the data. Overall, the 100% humidity data were lower in locations 4 and 5, dramatically lower in location 6, higher in location 1, and higher at the expected value in locations 2 and 3. Additionally, the shape of the data at all three humidity values matched the expected shape, leading to the conclusion that humidity is also not a significant factor in RFID tag performance.

The corrosion simulation experiment results showed that the correlation between the RSSI of RFID tags and the antenna length was very weak. Variance existed among different RFID tags; however, the results of the pristine RFID tag showed that the RSSI of a single tag would generally decrease upon the decrease of the antenna length, and no signal could be detected when the antenna was cut by more than 3 cm at both ends with a distance of 66 cm between the tag and reader. The on/off RFID smart tag was deactivated when both sides of the exposed parts of the antenna were cut, and no RSSI could be detected when the distance between tag and reader was larger than 1 cm.
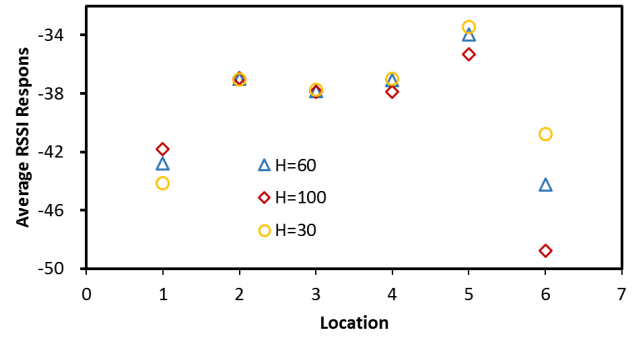
(a) On/Off RFID Tag at 25 ° C
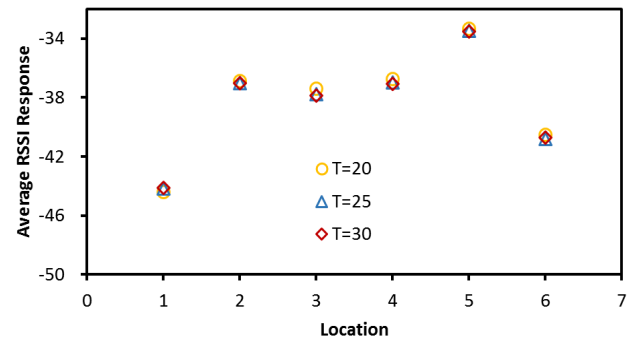
(b) On/Off RFID Tag at 30% Humidity

Figure 5. Effect of Temperature and Humidity on On/Off RFID Tag RSSI

In the corrosion simulation testing, the results did not follow a specific trend. In theory, any shortening of the antenna should have had a two-part effect. The first is that a shorter antenna length should decrease the strength of the response, following Equation (1). The second effect is detuning of the tag. Initially, the tags were tuned to absorb a specific projected frequency. If the frequency was increased or decreased, the tag would still absorb some of the signal, but the absorption efficiency would decrease. This detuning behavior complicated the data and could cause reverse trends in the data. In order to solve this issue, a focus was made on targeting the on/off response of the tags instead of looking at their RSSI in order to determine the extent of corrosion.

Based on the results from the corrosion simulation testing, the tag's on/off response was utilized. When antenna length was short, the tag response could not be detected. This behavior allowed the researchers to design the tag such that the response variable was a binary on/off status, as opposed to a continuous change of RSSI. The chip and antenna were coated in a corrosion-resistant polymer, leaving

only the part of metal antenna very close to the chip exposed to the corrosive environment. By allowing corrosion to take place only at these desired locations, the tag was able to operate in only two possible states. One state was having signal response, when none of the exposed metal sections were corroded; the other one had no signal response, when the exposed part was corroded.

The corrosion test of the on/off RFID smart tags in acid solutions showed that the tags in the 5% acid solution were killed after 52 hours, and the tags in the 2.5% acid solution were killed after 98 hours, as illustrated in Figure 6. The minimum RSSI detected in this experiment was -100 dB, indicating complete deactivation of the tag. The on/off RFID smart tag buried in acidified soil could still be detected after 31 days. The corrosion experiments confirm the results from the corrosion simulation experiments, which is that the tag will be deactivated when both sides of the exposed metal are fully corroded and that partial corrosion would not cause signal change. When one side was fully corroded, the signal would dramatically decrease.
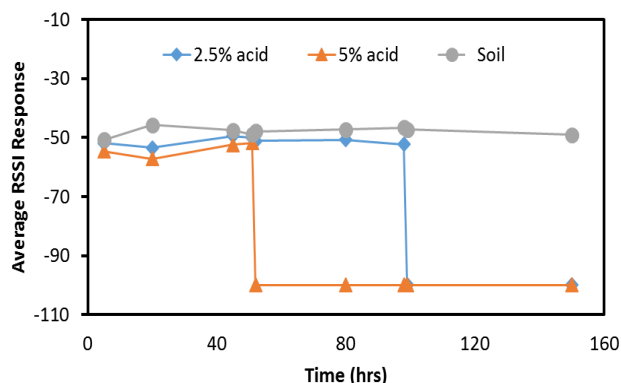
Figure 6. On/off RFID Tag Corrosion Test in Different Environments

Metal Coupon Experiments

The corrosion coupon experiments were conducted to optimize the tag design by estimating the expected trends in the vicinity of pipelines. The coupons were placed in acidified water and acidified soil to simulate the corrosion performance in different environments with a range of corrosive properties. Figure 7 depicts the dependence of corrosion rate on time and acid concentration. There was a sharp decrease in corrosion rate in the first few hours, after which the corrosion rate became more stable. It was observed that the stable rate of corrosion was dependent on acid concentration, with the 5% solution showing a higher rate (~ 8 mm/

year) compared to the 2.5% and 1.25% solutions (5 mm/year and 3.5 mm/year, respectively). The correlation between concentration and corrosion rate was established by the increased H^+ availability to the coupon leading to higher oxidation of the coupon. The anodic and cathodic reactions are given by Equations (2)-(4). Equation (3) takes place in acid solutions, while Equation (4) occurs in both moist air and liquid environments.

$$\text{Anode (oxidation): } Fe \rightarrow Fe^{2+} + 2e^- \qquad (2)$$

$$\text{Cathode (reduction): } 2H^+ + 2e^- \rightarrow H_2 \qquad (3)$$

$$O_2 + 2H_2O + 4e^- \rightarrow 2OH^- \qquad (4)$$
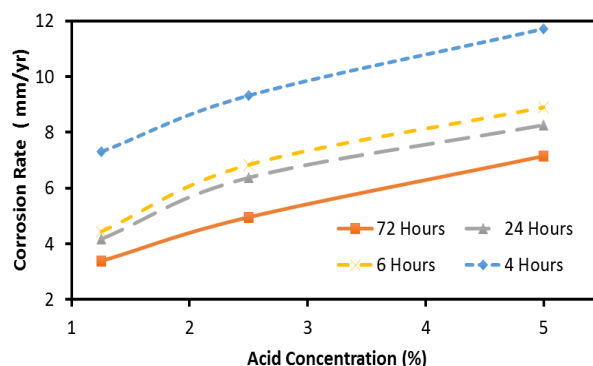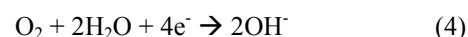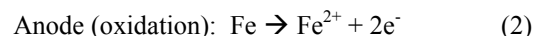
(a) Variation of Corrosion Rate with Concentration
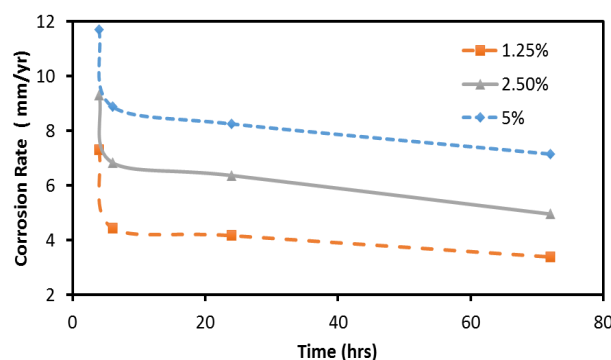
(b) Variation of Corrosion Rate with Time

Figure 7. Corrosion Rate of Metal Coupon in Acid Solution

The decrease in corrosion rate can be attributed to two factors: the consumption of reactants and the formation of a passive layer on the surface of the coupon, which impeded mass transfer. Because the system was not perturbed during the experiment, there was a non-homogenous distribution of ions, further limiting the corrosion reaction. The initial rate of corrosion could be attributed to the direct exposure of

uncoated and polished surfaces to the corrosive solution, providing an abundance of sites for corrosion to perpetuate; however, as the corrosion reaction proceeded, the coupon developed a thick layer of corrosion products on the surface. The formation of the corrosion product layer led to a decrease in reactant transport, causing the corrosion rate to drop and then stabilize as the equilibrium was reached between the rate of transport and the rate of reaction. In some applications, this passivated corrosion layer would slough off, exposing bare metal, which would cause the corrosion rate to spike. In these trials, however, the layer was attached well and no sloughing occurred, mainly due to the undisturbed and isolated environment in which the tests were performed. In service, normal ground movements and movements due to anthropological activity would lead to detachment of such passive layers and result in the exposure of bare metal.

Further trials used acidified soil to simulate realistic pipeline conditions, especially in soil which may have been subjected to acid rain or water runoff. The corrosion data from the acidified soil was plotted against time to estimate the trend for corrosion rate with time. Figure 8 shows the corrosion rates for both sets of acidification with time, and Figure 9 illustrates the surface degradation of the coupon after retrieval from the acidified soil. The corrosion rate of the metal coupons increased and then decreased with time for the soil acidified with the 1.25% acid, whereas the rate was stable for the soil with 0.5% acid and decreased with time for the 0.25% acidified soil. After more than 600 hours after the start of the test, the relatively low acidified soil (0.5%) displayed the highest corrosion rate, almost comparable to the rate that the highly acidified soil (10%) produced at the start of the experiment (~140 hours). The non-uniformity of the corrosion was also visually represented in the coupons, with Figure 9 illustrating the highly diverse distribution of corroded areas.

The main observation of these trials was that the visual corrosion pattern was highly non-uniform with little dependence on position or time. The randomness in corrosion location can be attributed to the consumption of the more corrosive substances in the soil, the formation of a passive protective film, and the differences in the conductivity of the microenvironments around the corrosion cells, given the variation of the compounds present in the soil. Even under relatively controlled conditions in the lab, and using soil taken from the same source, the trends of corrosion rate still showed significant differences. Moreover, as mentioned in the previous section, the corrosion was highly non-uniform; despite the decrease in the aggregate rate of corrosion, the formation of deep pits and indentations on the sample could lead to a pinhole failure in the pipeline.

The observations of the metal coupons support the corrodible RFID tag design. The RFID tags, if distributed in large enough numbers either underneath the pipe insulation or in the external environment, would help overcome the inherent randomness and unpredictability of the corrosion processes. Also, due to the nature of the RFID tag design, RFID tags can monitor corrosion in highly aggressive and extremely local environments (pitting-prone), and thus may work as proficient pitting corrosion detection sensors.
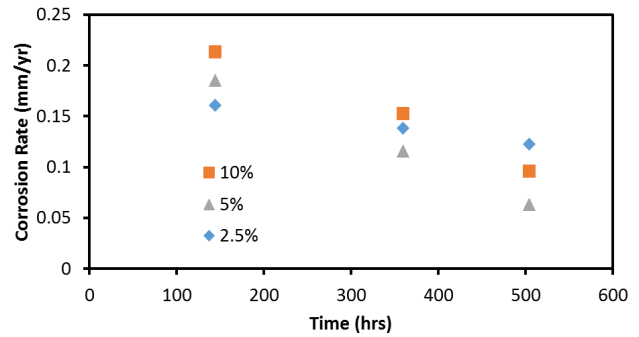
(a) Corrosion Rate of Acidified Soil for Set 1
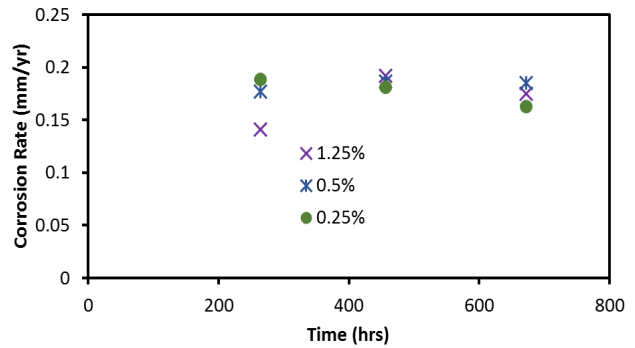
(b) Corrosion Rate of Acidified Soil for Set 2
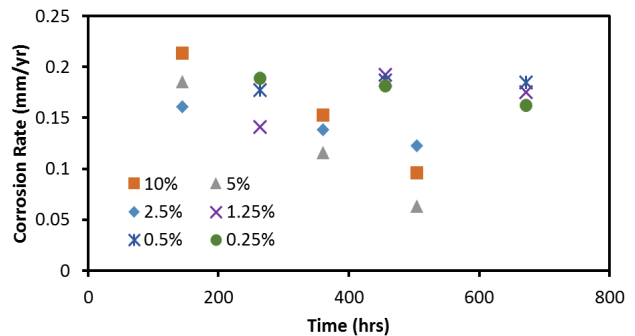
(c) Corrosion Rate of Acidified Soil for Both Sets 1 and 2

Figure 8. Corrosion Rate of Metal Coupon in Acidified Soil
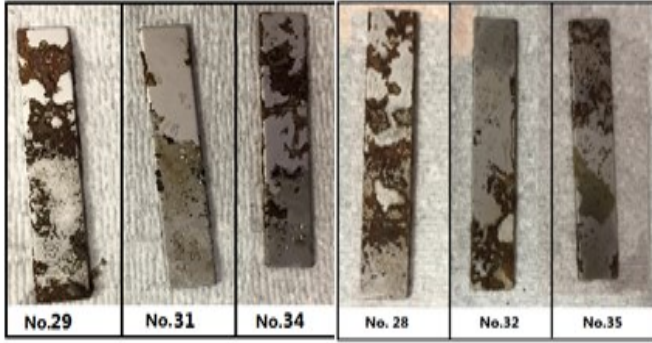
Figure 9. Non-uniformity of Corrosion in Soil (coupons 29, 31, and 34 are metal test coupons after being immersed for 360 hours; coupons 28, 32, and 35 are metal test coupons after being immersed for 144 hours)

Design Parameters

Important design parameters of the RFID tag were antenna length, thickness, surface/volume ratio, and material. Antenna length had an influence on the ability for the tag to receive a signal from the reader. Longer antennae would allow the chip to function further from the reader, which may be important depending on the scenario. Additionally, the antennae do not need to be straight; they can be constructed in a variety of different shapes depending on the need. Antenna thickness is important because it is the determining factor in corrosion time. The corrosion time of the antenna is dependent on the corrosive degree of the environment, the amount of material that must be corroded, and the exposed surface area on which corrosion can occur. Material to be corroded (volume) and exposed surface area can be reduced from three dimensions to a single cross section, assuming that corrosion takes place predominantly in the radial direction. This reduction in dimensions converts volume into cross-sectional area and surface area into circumference. Both of these parameters are functions of antenna thickness, assuming the antenna is a cylindrical wire. If information is known about the corrosivity of the environment into which the tag is being placed and the distance between the tag and the reader, then a tag can be designed for a specific application. However, if these variables are unknown, then a generic tag can be used and the parameters can later be adjusted, based on feedback from the field.

When these tags are placed in the field, the recommended configuration is a variety of tags with different thicknesses. By slightly changing their thickness, the tags can essentially be used as a clock. Assuming that the environment corrodes materials uniformly, then thinner tags will fail first, followed by thicker tags. The rate of tag failure can be used to determine the corrosivity of the environment and give an idea of the effective corrosion rate in the area. Table 3 gives the corrosion rate of different types of metals in different environments, as found in the literature. These corrosion-rate data can be used for the selection of antenna material and thickness. If, however, corrosion in the area is predomi-

Table 3. Corrosion Rate of Metal in Different Environments

#	Study	Material	Service	Corrosion Rate
1	Short term corrosion rates of copper alloys in saline groundwater [28]	C10100 Copper alloy	Synthetic 55g/L (TDS)	15.24 μm/y
		Copper	Brine A (300 g/L TDS)	71.12 μm/y
		Copper	Seawater 35 g/L TDS	50.8 μm/y
3	Corrosion monitoring under cathodic protection conditions (CMAS probes) [28]	Carbon steel (Type 1008, UNS G10080)	Drinking water	88.9 μm/y to 330 μm/y
		Stainless steel (Type 316L UNS S31603)	Drinking Water	0.17 μm/y
		Brass (Type 260 UNS C26000)	Drinking water	7.11 μm/y
4	Mildly corrosive soils [29]	Carbon steel	Mildly corrosive soil	11.94 μm/y
5	Corrosion rate in soil [30]	X42 Steel	Soil	5. 00 μm/y Electrochemical)
		X42 Steel	Soil	3.99 μm/y (gravimetric)
		X42 Steel	Soil rate + 1% NaCl	340.90 μm/y (Electrochemical)
		X42 Steel	Soil rate + 1% NaCl	363.98 μm/y (Gravimetric)

[*]μm/y = micrometers per year

nantly pitting or some other non-uniform type of corrosion, then the tags will not function as a clock, though they will still give an indication of a corrosive environment. This function can be used to help understand the corrosion phenomena in a particular area.

Conclusions

In this study, an environmental chamber was created for use in corrosion trials. This chamber was employed to conduct corrosion testing of RFID tags for potential pipeline applications. These experiments led to a novel RFID tag design that utilizes corrodible sections of the antenna to give the tag an on/off response. Additionally, corrosion coupons made of pipeline materials were used to relate the time to corrosion failure of the RFID tags to physical corrosion rates.

The initial RFID tag experimental results followed the expected trends, which served as a validation of the equipment used in these experiments. The flexibility of this technology makes it an ideal candidate for use in a variety of different areas. The main advantage of UHF RFID is that it has a very large scanning distance, over 15 meters, depending on the strength of the reader, the size of the antenna and chip, and the scanning environment. This long scanning range means that the tag can be buried or placed in locations that are not easily accessible and can be read remotely. To guarantee superior detection performance in this harsh environment, chips with industry leading sensitivity were selected and the chips protected by corrosion-resistive material. The operating temperature of the chip ranged from -50°C to 85°C. Two potential applications for the tags are for use with buried onshore pipelines and in monitoring pipeline corrosion under insulation (CUI). In buried pipeline applications, the tag can serve as an indicator of soil corrosivity and give an indication of the extent of corrosion that a pipeline would incur in the same environment. The tag would not need to be placed in direct contact with the pipeline, but could be buried nearby in order to give an accurate reflection of the soil. For use with CUI, the tag could be inserted under the insulation and remotely monitored without removing the insulation. Future work should include a real-world application of the RFID tags in order to better calibrate the rate of tag corrosion with the corrosivity of the soil.

Corrosion presents a serious problem from both an economic and a safety standpoint. Although corrosion-detection research has come a long way in recent years, it is still lagging behind the hazard of pipeline corrosion. The novel on/off design of the RFID chips provides a low-cost solution that is both easy to apply and free to maintain, bringing immense value to the field of corrosion.

References

[1] Schmitt, G. (2009). Global needs for knowledge dissemination, research, and development in materials deterioration and corrosion control. *New York, NY: The World Corrosion Organization*. Retrieved from http://www.finishingtalk.com/community/user-uploads/SFA/WCO%20White%20Paper.pdf

[2] Koch, G. H., Brongers, M. P., Thompson, N. G., Virmani, Y. P., & Payer, J. H. (2002). Corrosion cost and preventive strategies in the United States. Retrieved from https://www.nace.org/uploadedFiles/Publications/ccsupp.pdf

[3] U.S. Department of Transportation, Pipeline and Hazardous Materials Safety Administration, U.S. Department of Transportation. (2015). *Significant pipeline incident statistic from 1995 to 2014*. Retrieved from https://hip.phmsa.dot.gov/analyticsSOAP/saw.dll?Portalpages&NQUser=PDM_WEB_USER&NQPassword=Public_Web_User1&PortalPath=%2Fshared%2FPDM%20Public%20Website%2F_portal%2FSC%20Incident%20Trend&Page=Significant&Action=Navigate&col1=%22PHP%20-%20Geo%20Location%22.%22State%20Name%22&val1=%22%2

[4] Kishawy, H. A., & Gabbar, H. A. (2010). Review of pipeline integrity management practices. *International Journal of Pressure Vessels and Piping, 87*(7), 373-380.

[5] Pipeline and Hazardous Materials Safety Administration, Department of Transportation. (2014). *Code of Federal Regulations. Title 49 CFR Parts 100-199 (Transportation)*. Superintendent of Documents, Washington, DC: US Government Printing Office.

[6] American Society of Mechanical Engineers.(2011) . *ASME B31, Standards of Pressure Piping. ASME B31, 9*. Retrieved from http://www.engineeringtoolbox.com/asme-b31pressure-piping-d_39.htm

[7] Liu, H. (2003). *Pipeline engineering*. CRC Press.

[8] Manian, L., & Hodgdon, A. (2005). Pipeline integrity assessment and management. *Materials Performance, 44*(2), 18-22.

[9] Rankin, L. G. (2004). Pipeline integrity information integration. *Materials Performance, 43*(6), 56-60.

[10] Klechka, E. W. (2002). Pipeline integrity management and corrosion control. *Materials Performance, 41*(6), 24-27.

[11] Van Os, M. T., van Mastrigt, P., & Francis, A. (2006). An external corrosion direct assessment module for a pipeline integrity management system. *Paper presented at the 2006 International Pipeline*

Conference. Calgary, Alberta, Canada.

[12] Van Os, M., & van Mastrigt, P. (2006). A direct assessment module for pipeline integrity management at Gasunie. *Paper presented at the 23rd World Gas Conference.* Amsterdam.

[13] Moore, T., & Hallmark, C. (1987). Soil properties influencing corrosion of steel in Texas soils. *Soil Science Society of America Journal, 51*(5), 1250-1256.

[14] Castaneda, H., Alamilla, J., & Perez, R. (2004). Life prediction estimation of an underground pipeline using alternate current impedance and reliability analysis. *Corrosion, 60*(5), 429-436.

[15] Huang, J., Qiu, Y., & Guo, X. (2009). Analysis of electrochemical noise of X70 steel in Ku'erle soil by cluster analysis. *Materials and Corrosion, 60*(7), 527-535.

[16] Aung, N. N., & Tan, Y. J. (2004). A new method of studying buried steel corrosion and its inhibition using the wire beam electrode. *Corrosion Science, 46* (12), 3057-3067.

[17] Scully, J., & Bundy, K. (1985). Electrochemical methods for measurement of steel pipe corrosion rates in soil. *Materials Performance, 24*(4), 18-25.

[18] Sancy, M., Gourbeyre, Y., Sutter, E., & Tribollet, B. (2010). Mechanism of corrosion of cast iron covered by aged corrosion products: Application of electrochemical impedance spectrometry. *Corrosion Science, 52*(4), 1222-1227.

[19] Domdouzis, K., Kumar, B., & Anumba, C. (2007). Radio-Frequency Identification (RFID) applications: A brief introduction. *Advanced Engineering Informatics, 21*(4), 350-355.

[20] Koschan, A., Li, S., Visich, J. K., Khumawala, B. M., & Zhang, C. (2006). Radio frequency identification technology: applications, technical challenges and strategies. *Sensor Review, 26*(3), 193-202.

[21] Roberts, C. M. (2006). Radio frequency identification (RFID). *Computers and Security, 25*(1), 18-26.

[22] Cole, I., & Marney, D. (2012). The science of pipe corrosion: A review of the literature on the corrosion of ferrous metals in soils. *Corrosion Science, 56*, 5-16.

[23] Baker, M., & Fessler, R. R. (2008). *Pipeline corrosion.* Report submitted to the US Department of Transportation, Pipeline and Hazardous Materials Safety Administration, Office of Pipeline Safety.

[24] Materer, N. F., & Apblett, A. W. (2010). *Passive wireless corrosion sensor.* Google Patents. Retrieved from http://www.google.com/patents/US2009005842

[25] Griffin, J. D., Durgin, G. D., Haldi, A., & Kippelen, B. (2005). Radio link budgets for 915 MHz RFID antennas placed on various objects. *Paper presented at the Texas Wireless Symposium.* Austin, Texas.

[26] Rappaport, T. S. (1996). *Wireless communications: principles and practice* (Vol. 2). Prentice hall PTR New Jersey.

[27] Department of Defense. (2005). *Radio frequency identification – opportunities and challenges in implementation.* Washington DC. RFID Working Group.

[28] Davis, J. R. (2001). *Copper and copper alloys.* ASM international.

[29] Oshida, Y., & Guven, Y. (2015). Biocompatible coatings for metallic biomaterials. In book: *Surface Coating and Modification of Metallic Biomaterials*, 287. Woodhead Publishing.

[30] Cramer, S. D., & Covino, B. S. (2006). *Corrosion: Environments and Industries* (13). ASM International.

Biographies

YIZHI HONG is a research assistant of chemical engineering at Texas A&M University. He earned his BS (Chemical and Biological Engineering, 2011) degree from Zhejiang University, China. Mr. Hong may be reached at hongcome@tamu.edu

PRANAV KANNAN is a research assistant of chemical engineering at Texas A&M University. He earned his BS (Chemical Engineering, 2013) degree from the Institute of Chemical Technology (formerly UDCT), Mumbai, India. Mr. Kannan may be reached at pranav.kannan92@tamu.edu

BRIAN HARDING is a research assistant of chemical engineering at Texas A&M University. He earned his BS (Chemical Engineering, 2011) degree from Bucknell University. Mr. Harding may be reached at bzh001@tamu.edu

HAO CHEN is a risk engineer at DNV GL and was a research scientist in the Department of Chemical Engineering at Texas A&M University. He earned his BS (Chemical Engineering, 2007) degree from Tsinghua University, China, MS (Chemical Engineering, 2010), and PhD (Chemical Engineering, 2013) from the University of Michigan. His interests include developing chemical engineering solutions for advancing clean energy technology and improving energy and process safety. Dr. Chen may be reached at chen-hao@umich.edu

SAMINA RAHMANI earned her BS (Chemical Engineering 1997) degree from Bangladesh University of Engineering and Technology. She earned her PhD (Chemical Engineering 2002) degree from the University of Alberta. She was a research scientist (2013-2015) in the Mary Kay

O'Connor Process Safety Center, TAMU. Dr. Rahmani may be reached at samina.rahmani@mail.che.tamu.edu

BEN ZOGHI is Victor H. Thompson professor of electronic systems engineering, director of the RFID/Sensor laboratory and director for the office of engineering corporate relations. A member of the Texas A&M University faculty for 28 years, he has been Leonard & Valerie Bruce leadership chair professor, and Associate Department Head for Research in the Engineering Technology and Industrial Distribution Department at Texas A&M University. Ben's academic and professional degrees are from Texas A&M (PhD), The Ohio State University (MSEE), and Seattle University (BSEE). Dr. Zoghi may be reached at zoghi@tamu.edu

SAM MANNAN is a regent's professor and director of the Mary Kay O'Connor Process Safety Center. Before joining TAMU, he was vice president at RMT, Inc., a nationwide engineering services company. In that capacity, he was the national program manager for the Process Safety and Risk Assessment projects. His experience is wide-ranging, covering various aspects related to process design, process safety, and risk assessment in the CPI. Professor Mannan is the recipient of numerous awards and recognitions from AIChE, TAMU, and IChemE, including the recent Bush Excellence Award for Faculty in Public Service. Professor Mannan received his BS Ch.E. in 1983 and PhD in 1986 from the University of Oklahoma.

SUPPORT VECTOR MACHINES FOR FAULT IDENTIFICATION IN THREE-PHASE INDUCTION MOTORS

Sri Kolla, Bowling Green State University; Rama Hammo, Bowling Green State University

Abstract

In this paper, the authors present a technique for identifying faults in a three-phase induction motor, based on a support vector machine (SVM). In this study, the authors looked at external faults experienced by the induction motor. The SVM was trained to identify external faults using three-phase RMS currents and voltages from a 1/3 hp induction motor, collected in real-time by a data acquisition system. LIBSVM software was used for training and testing of the SVM. Results showed that the proposed SVM-based method was effective in identifying different external faults in the induction motor.

Introduction

The induction motor is one of the most important motors used in industrial applications. The motor may experience different faults, due to varying operating conditions. The main types of external faults range from single phasing to overload [1]. When a fault is experienced, the motor should be disconnected by monitoring it. Digital processor-based relays are generally used for this purpose [2]. Complex signal processing techniques are used in the relay logic for reliable and fast identification of these faults. Recent smart-grid developments allow for the application of artificial intelligence (AI) techniques for induction motor relays, which include artificial neural networks (ANN) [3]. The traditional neural networks approach has difficulties with generalization, and it can produce models that over fit the data. The support vector machine (SVM) method is becoming popular, due to many attractive features. This method was developed by Vapnik [4] and is based on statistical learning theory, which can improve generalization of the model.

Different stator fault monitoring techniques for induction motors were reviewed by Siddique et al. [5] and Ojaghi et al. [6], who published an extensive list of references on this topic. A fault detection and protection scheme based on a programmable logic controller (PLC) was also developed by Bayindir et al. [7]. The motor current signature analysis (MCSA) that analyzes high-frequency components to identify faults has been used by many researchers [8]. Chow and Yee [9] applied neural networks to detect incipient faults in single-phase induction motors in the early 1990s. They identified stator winding faults and bearing wear using motor current and speed as inputs. Kolla and Altman [10] used ANN for external fault identification in a three-phase induction motor in real-time. A fuzzy logic-based motor protection system was designed by Uyar and Cunkas [11]. Tan et al. [12] applied ensemble empirical mode decomposition (EEMD) in order to detect mechanical faults in an induction motor. The SVM techniques for identifying faults in induction motors have been recently proposed by Widodo and Yang [13], Poyhonen et al. [14], and Nguyen and Lee [15]. Fang and Ma [16] combined the MCSA and the SVM techniques in order to identify induction motor faults. Matic et al. [17] and Keskes et al. [18] applied SVM for diagnosis of broken rotor bars in motors. However, there has not been much work in applying SVM techniques to detect external faults in three-phase induction motors.

In this paper, the authors present an SVM-based technique to detect external faults in three-phase induction motors. Three-phase RMS current and voltage signals were used as inputs to train the SVM for identifying the faults. These signals were obtained from a LabVIEW-based data acquisition system from a 1/3 hp squirrel cage induction motor in real-time [10]. The LIBSVM program was used for training the SVM. The fault voltage and current signals from the induction motor were also used for testing the performance of the trained SVM.

Three-Phase Induction Motor Faults

Several types of external fault conditions may be experienced by a three-phase induction motor during its operation [1]. These faults include single phasing, unbalanced supply voltage, overload, locked rotor, over voltage, and under voltage. A brief account of these faults and the type of protection used for each of them was explained by Kolla and Varatharasa [3]. It can be observed that motor currents and voltages have unique features during faults [3, 10]. For example, three-phase voltages and currents for a single-phasing fault case are shown in Figure 1. It can be seen that the currents in two phases are 180° out of phase, and the third current is zero for this fault. These features are generally used by protective relaying schemes to detect different types of faults in induction motors [1].
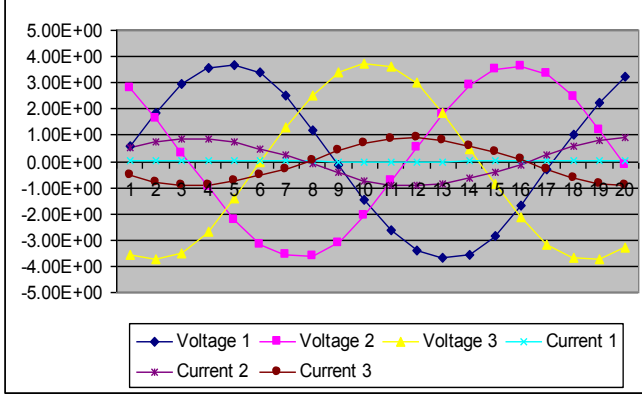
Figure 1. Three-Phase Voltages/Currents for Single Phasing Fault

Computer-based relay schemes were found in the literature to protect a motor under external fault conditions [1, 2]. Recently, there have been attempts to use AI techniques such as fuzzy logic and ANN to identify these faults [3, 11]. In this study, the authors further explored the use of AI techniques and applied SVM-based methods in order to identify external faults in three-phase induction motors.

Support Vector Machines

Support vector machines are a learn-by-example paradigm spanning a broad range of classifications and regression problems [19]. The technique was introduced by Vapnik [4] in the framework of statistical learning theory. The method relies on support vectors (SV) to identify the decision boundaries between different classes. The SVM employed for two class problems was based on hyperplanes to separate the data, as shown in Figure 2. A summary of the mathematical development of the SVM technique is given here.
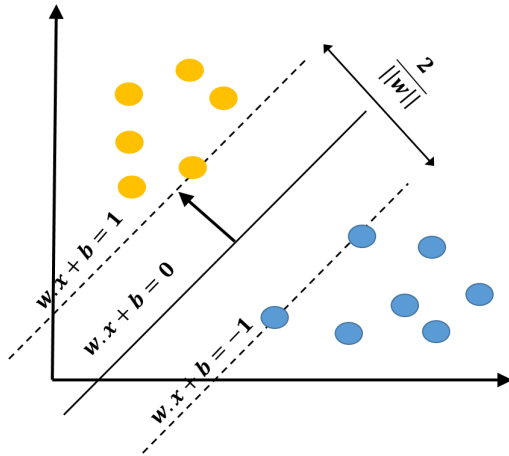
Figure 2. Linear Separating Hyperplane

Given a set of training samples $x_1, x_2, \ldots, x_m$ with outputs (labels) $y_1, y_2, \ldots, y_m$, the aim was to learn the hyperplane $\mathbf{w}.\mathbf{x} + b$, which separates the data into classes, as given in Equation (1), such that:

$$\begin{aligned} \mathrm{w.x}_i + b \geq 1 \; if \; y_i = 1 \\ \mathrm{w.x}_i + b \leq -1 \; if \; y_i = -1 \quad \forall i. \end{aligned} \tag{1}$$

The separating hyperplane which maximizes the margin (distance between it and the closest training sample) can be found by maximizing $2/\|\mathbf{w}\|$, subject to the constraints of Equation (1). This problem can be solved by a quadratic optimization method [4] and minimizing the objective function given in Equation (2):

$$\frac{1}{2}\|w\|^2 + c\sum_i \xi_i \tag{2}$$

subject to $y_i(\mathrm{w.x}_i+b) \geq 1-\xi_i, \xi_i \geq 0$, $1 \leq i \leq n$, where, ξ_i are the slack variables, which measure the miscalculation of the data x_i, and c is the error penalty constant.

The optimization problem can be solved by forming the Lagrangian, and it is easy to solve the dual problem [4]. After solving for $\mathbf{w}$ and b, a class to which a test vector $\mathbf{x}_t$ belongs is determined by evaluating $\mathbf{w}.\mathbf{x}_t+b$. This classification method is limited to linear separating hyperplanes. If the training data are beyond the boundary of the linear separation, a nonlinear classification can be applied by mapping the input data $\mathbf{x}$ into feature space $\phi(\mathbf{x})$ using mapping ϕ [4]. In an SVM-based linear classifier method, training data appear in the form of dot products $\mathbf{x}_i.\mathbf{x}_j$. For a nonlinear classifier, this translates into dot product $\phi(\mathbf{x}_i).\phi(\mathbf{x}_j)$ in the feature space. It is known that the kernel is a function $K(\mathbf{x}_i, \mathbf{x}_j) = \phi(\mathbf{x}_i).\phi(\mathbf{x}_j)$ that returns dot product in feature space, given two inputs [4]. By computing the dot product directly using the kernel function, the actual mapping $\phi(\mathbf{x})$ can be avoided, which may be difficult to find. There are several kernel functions available; choosing one depends on the training data of the problem being solved. The commonly used kernel functions are given in Equations (3)-(6) [19, 20]:

$$\text{Linear: } K(x_i, x_j) = x_i^T x_j \tag{3}$$
$$\text{Polynomial: } K(x_i, x_j) = (\gamma x_i^T x_j + r)^d, \gamma > 0 \tag{4}$$
$$\text{Radial Basis Function: } K(x_i, x_j) = \exp(-\gamma \|x_i - x_j\|^2), \gamma > 0 \tag{5}$$
$$\text{Sigmoid: } K(x_i, x_j) = \tanh(\gamma.x_i^T x_j + r) \tag{6}$$

where, r, d, γ are kernel parameters.

Of these, the radial basis function (RBF) kernel is one of the most popularly used functions in SVM applications. The SVM method discussed for two class problems can be extended for multiple classes using "one-against-one" and

"one-against-the-rest" strategies [19, 20]. There are several software programs, both commercial and freeware, available for implementing the SVM technique. In this current study, LIBSVM [20] software was used. The program comes with different tools to train and test data to classify, as well as other functions such as svm-train, svm-scale, svm -predict, and svm-toy. These functions allow selection of different kernel functions such as RBF and several parameters that can be varied such as c and γ in order to facilitate the training of the data.

SVM for Detecting Induction Motor Faults

The inputs and outputs for the SVM should be selected as the first step for identifying fault and no-fault conditions in the induction motor. In this study, RMS values of three-phase voltages and currents were selected as inputs. This resulted in six inputs to the SVM. The data were classified into seven output values, corresponding to six fault conditions (described previously) and a no-fault condition. The outputs were numbered from 1 to 7, and the corresponding number was obtained from the SVM if that particular condition exited. Figure 3 illustrates the inputs (RMS voltages and currents) and outputs (faults and no-fault conditions) of the SVM.
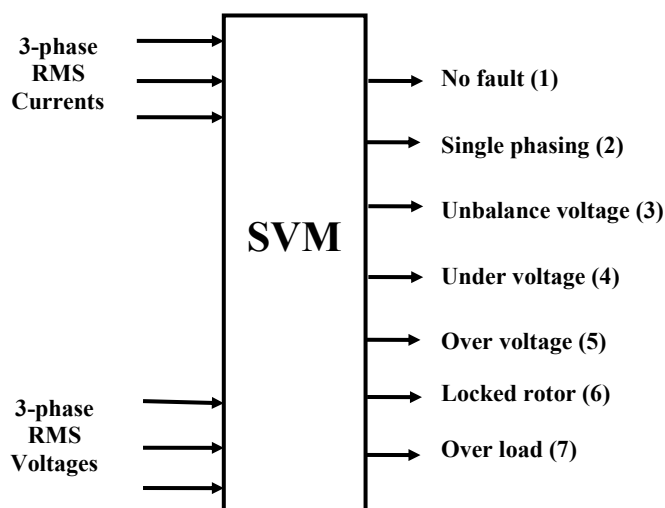
Figure 3. SVM to Detect Induction Motor External Faults

The next step in using the SVM for identifying fault conditions was to train it. The voltage and current waveforms representing the six different fault conditions and the no-fault condition were considered. These waveforms were obtained in real-time from a 1/3 hp, 208 V, three-phase squirrel cage induction motor, as described in the study by Kolla and Altman [10]. Three variacs were used to implement under-voltage, over-voltage, and unbalanced supply voltage faults. Overload and locked-rotor fault conditions were created by a prony brake. A single phasing fault was created by disconnecting a phase power line. The data associated with these faults were collected in real-time using LabVIEW. The voltage and current waveforms for an over-voltage fault are shown in Figure 4; similar waveforms were obtained for other faults.
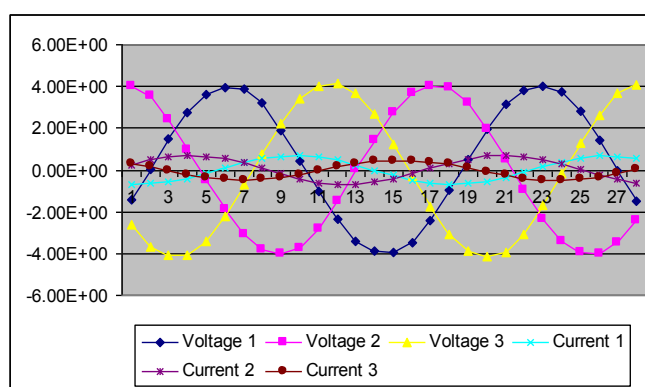
Figure 4. Voltages and Currents for Over-Voltage Fault

Figure 5 shows the data acquisition system that was used to collect the voltage and current samples. The signal conditioning system reduced the three-phase voltages and converted three-phase currents into their proportional voltages. The conversion range was +/- 10 V, the scaling factor for voltages was 41.283 V/V, and the factor for current-to-voltage conversion was 2.3741 A/V. Low-pass filters were used for anti-aliasing purposes and the signals were passed to the National Instruments' SCXI 1000 chassis shown in Figure 5. The SCXI chassis contained a simultaneous sampling analog module 1140 to collect the voltages. The chassis communicated with a PCI-MIO-16E-1 multifunction I/O card in the computer.
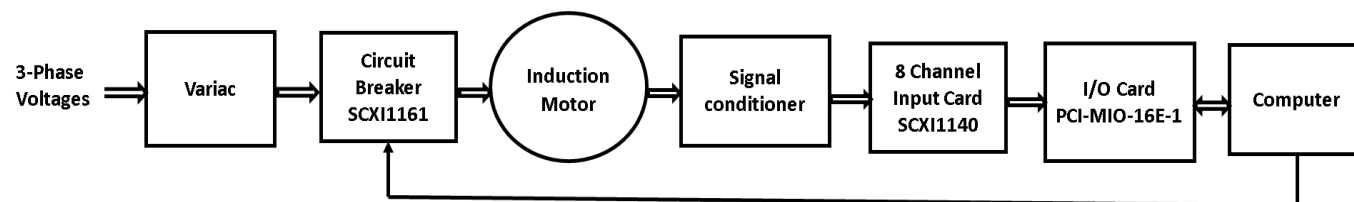
Figure 5. Induction Motor Data Acquisition System

LabVIEW was used to acquire the instantaneous motor voltage and current data from the signal conditioners. The program acquired the data simultaneously at a sampling rate of 1000 scans/sec. The instantaneous signals were then converted to RMS values. To train and test the SVM-based fault identification system, these RMS values were used. The number of signals used to train the SVM for each fault type is listed in Table 1. These represented a total of 788 cases for the different faults.

Table 1. Training Data Signals

Condition (fault/no fault)	Number of Signals
No Fault (NF)	154
Single Phasing (SP)	85
Unbalanced Voltage (UB)	450
Under Voltage (UV)	49
Over Voltage (OV)	10
Locked Rotor (LR)	10
Overload (OL)	30
Total Signals	788

The SVM was trained using the svm-train tool of LIBSVM [20]. Before training, the data were scaled with two different scaling values between (-1, 0) and (-1, 1) using the svm-scale tool. A kernel function and other parameters that could impact performance were selected to train the SVM. The values for c and parameter γ were determined using the grid search tool called grid.py. The trained SVM was tested with data sets consisting of data used for training and a set of 21 data that was not used for training. These test data sets were used in the svm-predict tool of LIBSVM.

Training and Testing Results for Detecting Induction Motor Faults

The training of the SVM was first accomplished using RBF as the kernel function, and 788 signals of the three-phase induction motor data explained in the previous section. The testing was performed by using the 21 samples that were not part of the training, in addition to data used for training. Optimization of the kernel parameters was achieved using the grid search tool of LIBSVM. Different scaling factors for the data were also used in the training process. The first case considered was to apply the RBF kernel with a scaling range between (-1, 1). After searching for the best parameter values for γ and c using grid.py, the optimum values obtained were (C=128, γ =0.5). Figure 6 shows the search results. However, the classification accura-

cy obtained for the untrained data with these parameter values was only 90.47% (19/21 samples).
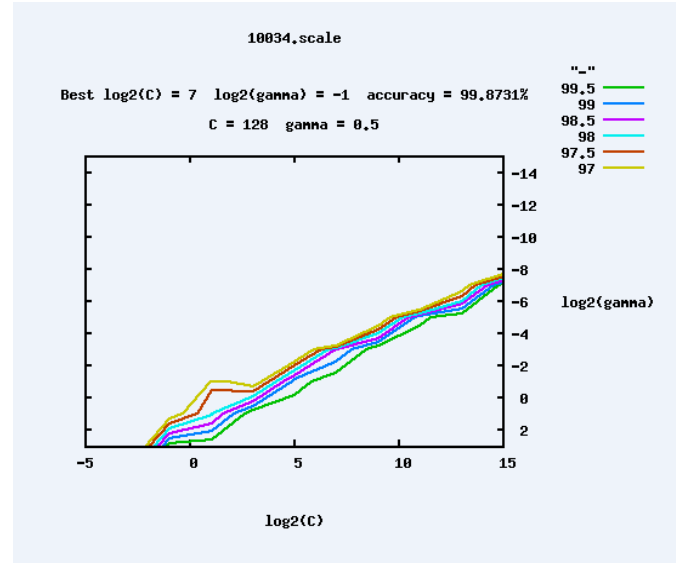
Figure 6. Search Output of Optimum Values for C and γ for (-1, 1) Scaling

Since the classification accuracy was not 100% with this scaling, a second case was considered using the same RBF kernel function with a different scaling range between (-1, 0). For this case, the optimum kernel parameters were found to be (C=512, γ =0.5). The search results are shown in Figure 7. The classification accuracy (testing) was found to be 100% for the 21 samples of untrained data for this case. The classification accuracy was 100% for both scaling cases when the trained data of 788 used for testing.
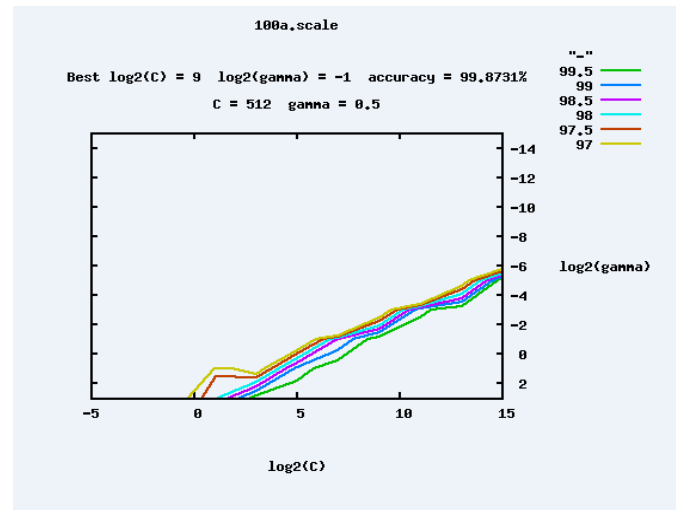
Figure 7. Search Output of Optimum Values of C and γ for (-1, 0) Scaling

The input voltage and current waveforms for one of the sets used to test the SVM are shown in Figures 1, 4, 8, and 9. Figure 1 shows the voltage and current waveforms from a single phasing fault case, while Figure 4 shows the waveforms from an over-voltage fault. Figure 8 shows the waveforms for a no-fault case. According to Figures 4 and 8, the three-phase voltage amplitudes occurred more often in the over-voltage case than the no-fault case. Figure 9 shows the waveforms from an unbalanced voltage fault, where all three voltages and currents had unequal amplitudes and phase angles. Similar waveforms were obtained for under-voltage, overload, and locked-rotor cases. RMS values of voltages and currents for all of these cases were calculated and are reported in Table 2. The third row for each of the fault cases in the table corresponds to these seven voltage and current waveform figures. The table also shows another two sets of data that were used as a part of the data to test the performance of the SVM. It can be seen from the table that the seven types of conditions were correctly identified by the proposed SVM method for these three sets of data that were not used in training.
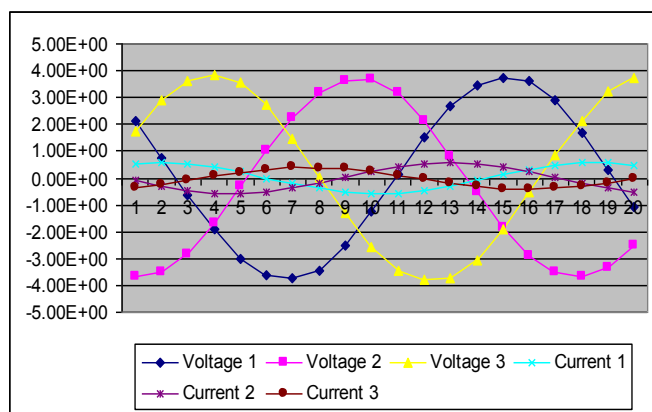
Figure 8. Voltages and Currents for the No-Fault Condition
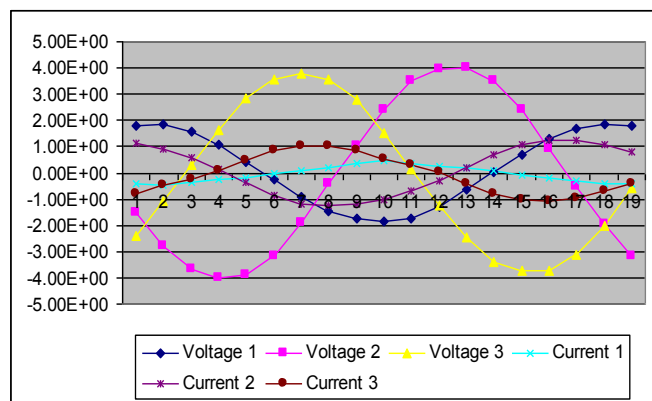
Figure 9. Voltages and Currents for the Unbalanced Voltage Fault

Table 2. Testing Results of the SVM

Faults	Inputs						Out-puts
	V1	V2	V3	I1	I2	I3	
No Fault (1)	2.650	2.640	2.696	0.428	0.428	0.431	1
	2.694	2.652	2.690	0.517	0.521	0.502	1
	2.622	2.614	2.666	0.410	0.418	0.417	1
Single Phasing (2)	2.688	2.609	2.721	0.625	0.629	0.013	2
	2.694	2.642	2.703	0.644	0.648	0.004	2
	2.616	2.600	2.642	0.628	0.632	0.004	2
Unbalanced Voltage (3)	2.624	1.906	2.022	0.538	0.249	0.332	3
	1.682	2.475	2.702	0.186	0.634	0.628	3
	1.624	2.019	2.585	0.207	0.449	0.576	3
Under Voltage (4)	1.088	1.087	1.084	0.231	0.239	0.225	4
	1.966	1.969	1.977	0.305	0.318	0.300	4
	1.976	1.967	1.995	0.306	0.312	0.307	4
Over Voltage (5)	2.888	2.878	2.863	0.482	0.499	0.496	5
	2.856	2.839	2.871	0.478	0.477	0.467	5
	2.882	2.872	2.868	0.488	0.484	0.459	5
Locked Rotor (6)	2.657	2.613	2.687	1.671	1.651	1.669	6
	2.649	2.614	2.647	3.090	3.096	3.043	6
	2.573	2.565	2.609	3.052	3.073	2.996	6
Over-load (7)	2.638	2.602	2.675	0.807	0.788	0.800	7
	2.681	2.639	2.679	0.831	0.833	0.820	7
	2.604	2.600	2.643	0.882	0.893	0.884	7

The effect of different kernel functions on classification accuracy was also studied using the 21 test samples. The kernel functions considered were linear, polynomial, RBF, and sigmoid. The effect of different scaling factors and the grid search usage on these different kernel functions was also considered in this study. Table 3 presents different kernel function classification accuracy with different scaling factors and grid search modifications for C and γ values. It was found that the RBF with the scaling between (-1, 0) gave the classification accuracy of 100%, as discussed previously. Also, similar results were achieved by the polynomial kernel function when the scaling was between (-1, 1), which gave a testing classification accuracy of 100%.

Table 3. Effect of Different Kernel Functions

Kernel Function Type	Scaling Factor	Grid Search Effect	Classification Accuracy
Linear Kernel Function T=0.	(-1, 0)	No mod.	33.3%
		Mod. C=512, γ =0.5	71.42%
	(-1, 1)	No mod.	57.14%
		Mod. C=128, γ =0.5	71.42%
Polynomial Kernel Function. T=1.	(-1, 0)	No mod	28.57%
		Mod. C=512, γ =0.5	95.23%
	(-1, 1)	No mod	33.33%
		Mod. C=128, γ =0.5	100%
Radial Bases Function. T=2.	(-1, 0)	No mod	33.33%
		Mod. C=512, γ =0.5	100%
	(-1, 1)	No mod	33.33%
		Mod. C=128, γ =0.5	90.47%
Sigmoid Kernel Function T=3.	(-1, 0)	No mod	19.04%
		Mod. C=512, γ =0.5	28.57%
	(-1, 1)	No mod	33.3%
		Mod. C=128, γ =0.5	38.095%

Conclusions

An application of an SVM method for identifying external faults in a three-phase induction motor was presented in this paper. The authors also described different parameters used for training the SVM, along with testing results using fault data collected in real-time from a 1/3 hp three-phase induction motor. The effect of various kernel functions and scaling of data on training and testing of the SVM were studied and found to influence fault identification. The RBF kernel in this study was found to be effective in identifying induction motor external faults. It was observed that the time required for the model creation phase with the SVM method was less than the ANN method, and SVM method accuracy was better than the ANN-based method [10]. RMS values of voltages and currents were used as inputs. Instantaneous values of voltages and currents may be directly used as inputs in future studies.

References

[1]   Elmore, W. A. (2004). *Protective Relaying Theory and Application*, 2nd ed., New York: Marcel Dekker, Inc.

[2]   Phadke, A. G., Thorp, J. S. (2009). *Computer Relaying for Power Systems,* 2nd ed, England: John Wiley&Sons.

[3]   Kolla, S. R., Varatharasa, L. (2000). Identifying three-phase induction motor faults using artificial neural networks, *ISA Transactions*, *39*, 433-439.

[4]   Vapnik, V. N. (1998). *Statistical Learning Theory*, New York: John Wiley&Sons.

[5]   Siddique, A., Yadava, G. S., Singh, B. (2005). A review of stator fault monitoring techniques of induction motors. *IEEE Transactions on Energy Conversion*, *20*, 106-114.

[6]   Ojaghi, M., Sabouri, M., Faiz, J. (2014). Diagnosis methods for stator winding faults in three-phase squirrel-cage induction motors. *International Transactions on Electrical Energy Systems*, *24*, 891-912.

[7]   Bayindir, R., Sefa, I., Colak, I., Bektas, A. (2008). Fault detection and protection of induction motors using sensors. *IEEE Transactions on Energy Conversion*, *23*, 734-741.

[8]   Benbouzid, M. E. H., Kliman, G. B. (2003). What stator current processing-based technique to use for induction motor rotor faults diagnosis. *IEEE Transactions on Energy Conversion*, *18*, 238-244.

[9]   Chow, M. Y., Yee, S. O. (1991). Using neural networks to detect incipient faults in induction motors. *Journal of Neural Network Computing*, *2*, 26-32.

[10]   Kolla, S. R., Altman, S. D. (2007). Artificial neural network based fault identification scheme implementation for a three-phase induction motor. *ISA Transactions*, *46*, 261-266.

[11]   Uyar, O., Cunkas, M. (2011). Design of fuzzy logic based motor protection system. *Proc. 6th International Advanced Technologies Symposium,,* Elazig, Turkey.

[12]   Tan, L., Mussa, A., Poling, J., Justice, K., Xu, H. (2014). Rotational machine fault detection with ensemble empirical mode decomposition based on a three-orthogonal channel sensor. *International Journal of Engineering Research and Innovation*, *6*, 33-40.

[13]   Widodo, A., Yang, B.-S. (2007). Support vector machine in machine condition monitoring and fault diagnosis. *Mechanical Systems and Signal Processing*, *21*, 2560-2574.

[14] Poyhonen, S., Arkkio, A., Jover, P., Hyotyniemi, H. (2005). Coupling pairwise support vector machines for fault classification. *Control Engineering Practice*, *13*, 759-769.

[15] Nguyen, N. T., Lee, H. H., (2008). An application of support vector machines for induction motor fault diagnosis with using genetic algorithms. *Proceedings of the ICIC*, Berlin: Springer-Verlag,, 190-200.

[16] Fang, R., Ma, H. (2006). Application of MCSA and SVM to induction machine rotor fault diagnosis. *Proc. of the 6th World Congress on Intelligent Control and Automation, IEEE,* Dallan, China, 5543-5547.

[17] Matic, D., Kulic, F., Pineda-Sanchez, M., Kamenko, I. (2012). Support vector machine classifier for diagnosis in electrical machines: Application to broken bar. *Expert Systems with Applications*, *39*, 8681-8689.

[18] Keskes, H., Braham, A., Lachiri, Z. (2013). Broken rotor bar diagnosis in induction machines through stationary wavelet packet transform and multiclass wavelet SVM. *Electric Power Systems Research*, *97*, 151-157.

[19] Ravikumar, B., Thukaram, D., Khincha, H. P. (2009). An approach using support vector machines for distance relay coordination in transmission system. *IEEE Transactions on Power Delivery*, *24*, 79-88.

[20] Chang, C. C., Lin, C. J. (2010). LIBSVM: A library for support vector machines. Software available at http://www.csie.ntu.edu.tw/~cjlin/libsvm.

Biographies

SRI KOLLA is a professor in the Electronics and Computer Engineering Technology Program at Bowling Green State University since 1993. During 2008-2009, he was a Fulbright Research Scholar in the Electrical Engineering Department, Indian Institute of Science, Bangalore. He was also a guest researcher at the Intelligent Systems Division, National Institute of Standards and Technology, in Gaithersburg, MD, 2000-2001. He was an assistant professor at Pennsylvania State University, 1990-1993. Dr. Kolla earned his PhD from the Electrical Engineering and Computer Science Department of the University of Toledo in 1989. His teaching and research interests include electrical engineering/technology with specializations in artificial intelligence, control systems, computer networks, and power systems. He is a fellow of IE (India), senior member of IEEE and ISA, and a member of ASEE and ATMAE. Dr. Kolla may be reached at skolla@bgsu.edu

RAMA HAMMO received his master's of Technology Management degree in Engineering Technology from Bowling Green State University in 2014. He received his bachelor's degree in Electrical Engineering from the University of Musel, Iraq, in 2006. He worked as a business manager in the Marketing and Communication Department of Al-Hazem Company, Iraq, for two years. He is a member of the Bloomsbury Honor Society. His areas of interest include artificial intelligence, computer software, electronic communication, and automation. Mr. Hammo may be reached at rhammo@bgsu.edu

CONTINUOUS CONTROL DESIGN IN PREDATOR-PREY NATURAL RESOURCE SYSTEMS

Dale B. McDonald, Midwestern State University

Abstract

The primary objective of this treatment was the design of a control (harvesting) effort for a ratio-dependent predator-prey system. The hope was to allow the harvesting of the prey, while dictating suitable biomass equilibrium levels to maintain a healthy natural resource system. Further contributions included the development of the control law by manipulating its time rate of change. This was done in order to mitigate parasitic behaviors such as "chatter" and "finite time interval switching control" which, while mathematically feasible, were physically inappropriate. Numerical simulations incorporated gains on the two terms, which describe the control algorithm. One term (including the gain) promotes convergence to desired biomass levels. The second term (and associated gain) mitigates the potential for undesired behavior of the controlled system. In total, the usefulness of the algorithm, given uncertainty in the predator-prey dynamics, was proven.

Introduction

The reality is that natural resources, whether water, energy, food, or the like, are becoming more critical areas of study for obvious reasons. This places a large, important burden upon those practitioners wishing to develop, in this case, harvesting (control) algorithms in which humans interact with predator-prey natural resource systems. It is important to recognize that harvesting algorithms, as with any control algorithm, are dependent upon the quality of the information available. The purpose of this treatment was to demonstrate that manipulating the time rate of change of the control, in this case the time rate of change of the harvesting effort, allowed for the implementation of a strategy that is much more reasonable to implement, both mathematically and physically. In particular, three prior studies provided the foundation and motivation for this current study.

In a study by McDonald [1], it was found that response surface methodology might be used to estimate ecological parameters for ratio-dependent predator-prey natural resource systems. The right-hand side of the predator-biomass time rate of change was sampled then reconstructed with response surface models (RSMs) via radial basis functions (RBFs). Ultimately, it was found that for specific RSMs and RBFs, parameters within the ratio-dependent predator dynamics could be accurately estimated. This was achieved during the derivation and application of the so-called instantaneous maximization of net economic revenue (IMNER) algorithm that considered economic and biomass level concerns. A similar algorithm, instantaneous optimization of net revenue harvesting (IONRH), was applied to a prey-dependent predator-prey natural resource system [2]. Its purpose was to provide for sustainable harvesting of the fundamentally different ecological system. In another study by McDonald [3], it was found that sensitivity of such developed RSMs, used in parameter estimation, could detect more accurate parameter estimates.

As observed in these prior studies [1, 2], it is clear that any harvesting algorithm that is acting upon gathered information and an assumed mathematical model must consider broader implications. Human expansion stresses natural resources of all types; the focus of this current treatment was upon predator-prey natural resource systems, where the predator is protected while the prey is not. Clearly, sustainable levels of both predator and prey must be maintained. This is not just for the health of the ecosystem; depletion of natural resources ultimately results in the collapse of economic concerns, employment, and reverberates throughout the natural and socio-economic spheres. The literature illuminates such notions.

In a study by Goh [4], the author discussed concepts such as natural resource management, including maximum sustainable yield harvest and the non-vulnerability of natural resource systems. Control algorithms, including optimal control strategies, were analyzed. Measures of total discounted net economic revenue and bionomic equilibrium for an unregulated fishery were considered. Additional efforts concerned economic and ecologic concerns such as the bioeconomic analysis of systems subject to harvest [5]. This was developed to describe a relationship between biological and economic equilibrium, where boundedness and stability were analyzed. The literature clearly displays the broad implications of the present analysis. In what follows, new interpretations, based in part upon IMNER but developed and implemented in drastically different means, prove to supply a much more physically reasonable control (harvesting) algorithm. Several interesting examples illustrate the utility.

It will be shown that methods that rely upon modifying the control effort directly are not robust to chatter, once uncertainties or disturbances are introduced into the system. This means that a fundamental shift in the manner in which control methods are developed must be illuminated. To avoid parasitic entities such as chatter, or in the continuous time sense, finite time interval switching control (FTISC), a new mechanism must be developed. It was revealed that the notions of sensitivity and control damping provide the solutions, which mitigate undesirable chatter (and/or FTISC) which results in pragmatic and useful control algorithms for a large variety of applications.

Dynamic System Model

Shown in Equation (1) is a variant of the Holling-Tanner predator-prey model, which was examined by other researchers [6-8]:

$$\dot{x}_1 = rx_1\left(1 - \frac{x_1}{K}\right) - \frac{\beta x_1 x_2}{\alpha + x_1} - qux_1 + \Delta$$

$$\dot{x}_2 = sx_2\left(1 - \frac{x_2}{vx_1}\right)$$

(1)

where, x_1 is the prey biomass and x_2 the predator biomass.

For the predator and prey, respectively, s and r denote the intrinsic growth rates. In the second of the two equations, v dictates the ratio of predator biomass to prey biomass, if a steady state or equilibrium condition is achieved [8]. For the prey, K is the carrying capacity, α is the half saturation level, β is the maximum harvesting rate, and q is the catchability coefficient. Due to the physical reality, that harvesting effort satisfies $0 \leq u \leq u_{max}$, the harvesting effort term u attached to Equation (1) is contained in the prey dynamics. This implies that the predator is not subject to harvest (protected) while the prey is not.

Note the term Δ in Equation (1); this represents some uncertainty in the system dynamics (for the prey biomass time rate of change). It is fair to say that a given mathematical model will affect the evolution of the state (or biomass). Of extreme importance is to note that Δ is unknown to the control algorithm; with Δ being a nonzero number, no control algorithm will have knowledge of this.

Control Law Foundations

The presence of uncertainty, Δ, in Equation (1) causes a problem for certain control (harvesting) algorithms. For the IMNER algorithm [1], it was beneficial that, when biomass conditions permit, minimum or maximum harvest was permitted. However, a scenario existed between these limits which was analogous to singular control and allowed for harvesting (with the employment/economic benefits thereof) to continue. This came with one caveat: perfect knowledge of an associated switching surface was needed to ensure that the control (harvesting) effort did not instantaneously switch from minimum to maximum effort. While mathematically permissible, this type of discontinuous control is not physically reasonable. Before proceeding to the derived algorithm, a review of the IMNER algorithm is presented.

Imner Algorithm

Summarizing from the work by McDonald [1], the IMNER algorithm acts instantaneously to maximize net economic revenue at each instant. The result of this, Equation (2), was the specification that (notice the control u, not its time derivative) necessary conditions for this maximization was satisfied if:

$$\begin{aligned} u &= u_{min} \quad if \quad \sigma > 0 \\ u &= u_{max} \quad if \quad \sigma < 0 \\ u &= u_s \quad if \quad \sigma = 0 \end{aligned}$$

(2)

where, σ is given by Equation (3):

$$\sigma = -\left(q\left(p - \tau\right)x_1 - C\right)$$

(3)

where, p is the price per unit biomass of the prey, q is still the catchability coefficient, τ is the rate of taxation, and C is the cost of fishing per unit effort.

Of particular attention is the intermediate control effort, u_s. This "singular" control actually dominated [1]; it represents an equilibrium control, where $\sigma \equiv 0$, implying that $\sigma = \dot{\sigma} = \ddot{\sigma}$ are identically zero. It was shown that this control regime allowed for continual harvesting outside of maximum or minimum control efforts. This result was pleasing. Maximum, minimum, or the intermediate control u_s coexisted in a manner that was physically appropriate; that is, instantaneous switching of the harvesting effort did not occur, which is what must happen in practice.

IMNER Considerations

In the current treatment, the real possibility that the control algorithm does not have access to perfect information had to be considered. Two fundamental issues were present in this case: the equilibrium condition $x_2 = vx_1$ will not occur exactly. This is not a major concern, as it is doubtful that given available technology/resources that any "sensors"

could perfectly predict biomass. What is more concerning is that the control or harvesting algorithm must act upon such information, and unwanted behavior may present. To illustrate this, consider example one.

Example One

This example illustrates the uncontrolled behavior of the system, Equation (1), and is free of any disturbance (i.e., $\Delta = 0$). The purpose is to understand the behavior of the system when prey is not subject to harvest. For illustration, let the initial prey biomass $x_1 = 50$ and the predator biomass $x_2 = 100$. Now let r = 1.5, K = 200, $\beta = 0.1$, $\alpha = 10$, q = 0.01, s = 1.2, $v = 5$, p = 10, $\tau = 3.21$, C = 7, $u_{max} = 0$, and $u_{min} = 0$. Note that with $u_{max} = u_{min} = 0$, the system evolves without any harvesting pressure. Figure 1 shows that the predator and prey achieve equilibrium values of $x_1 = 137.84$ and $x_2 = 689.22$, which are higher than what is expected in the presence of harvest, given by $\sigma = 0$. Note that the ratio of these equilibrium values is very near $v = 5$.
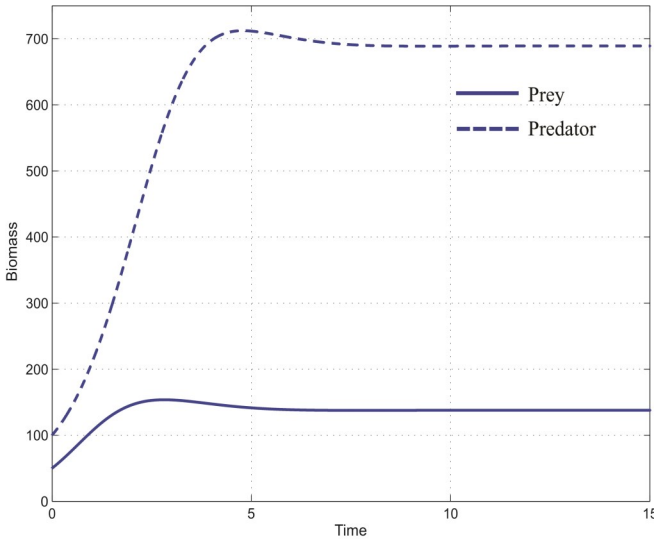
Figure 1. Prey and Predator Biomass versus Time

Once the behavior of the system, in the lack of harvest, is understood, it is important to robustly quantify system behavior once the control effort is implemented. To this end, note from Equation (3) that $\sigma = 0$ yields equilibrium biomass values:

$$x_1^* = \frac{C}{q(p-\tau)} = 103.09 \qquad (4)$$

and, with $v = 5$:

$$x_2^* = vx_1 = 5(103.09) = 515.45 \qquad (5)$$

Example Two

This example illustrates the IMNER algorithm with perfect information juxtaposed with imperfect information. First, let $\Delta = 0$, then implement the IMNER algorithm. Throughout this treatment, parameter values used are as stated in Example One with $u_{min} = 0$ and $u_{max} = 75$. Figure 2 displays the results at equilibrium; $x_2 = 515.46$ and $x_1 = 103.09$, where the ratio of x_2 to x_1 is very nearly five (numerical value of v), which is clearly seen in the figure. Notice the control law, which begins at maximum harvesting effort and transitions into continuous singular control.
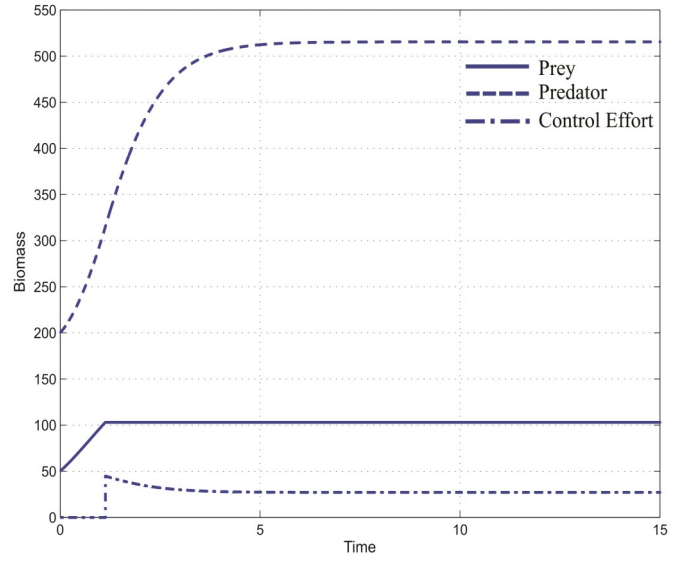
Figure 2. Prey and Predator Biomass versus Time (with harvesting effort)

It is fair to say that such a control law may reasonably be implemented in practice, based upon the numerical results. Now consider some nonzero disturbance ($\Delta \neq 0$) and implement the IMNER algorithm from Equation (2). The issue with Equation (2) is that, in order to provide for u = u_s, it is required that $\sigma \equiv 0$, which implies that $\dot{\sigma} = \ddot{\sigma} = \dots = 0$. This presents a problem: with $\Delta \neq 0$, the control algorithm has incomplete knowledge and cannot enforce this condition. Consider implementing Equation (2) to control the system Equation (1), where the control acts upon information that $\Delta = 0$ when, in actuality, $\Delta \neq 0$. Figure 3 displays the results with $\Delta = 0.1$; notice that $x_2 = 515.50$ and $x_1 = 103.10$ in the steady state.

The ratio of x_2 to x_1 is very nearly five, which is clearly seen in the figure. However, it is the control law that is the issue. This seemingly small uncertainty in the biomass (state) equations produces a control algorithm that suggests

that the harvesting effort should "chatter" between mini-
mum and maximum levels. This is not desirable and not
implementable in practice.
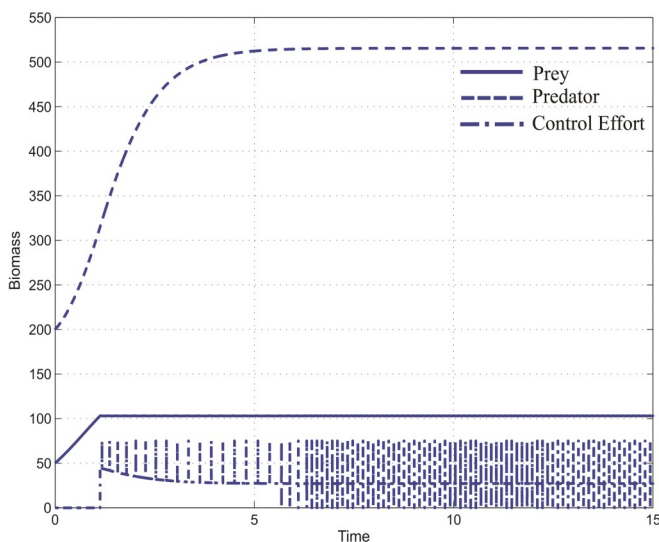
**Figure 3. Prey and Predator Biomass versus Time
(with harvesting effort and including the presence of chatter)**

Harvesting (Control) Methods

What is needed is another strategy. Specifying the control
(harvesting) effort directly, while avoiding unwanted behav-
ior, requires perfect knowledge of the system dynamics. The
remaining portion of this treatment will be devoted to illus-
trating that modifying the time rate of change of the control
is a better strategy. This method is partially inspired by
McDonald [9]. That study developed so-called "control
damping" algorithms. The idea was to develop control laws
that, of course, considered the control objective, optimiza-
tion of an objective function, and practical concerns.

These practical concerns included what is termed "finite
time interval switching control" (FTISC). This is analogous
to the chatter observed in Figure 3, but in a continuous time
sense. That is, the discontinuous chatter is replaced by a
(nearly) infinite frequency oscillation in the control effort
that is just as impractical to implement. In this same study
[9], a control algorithm was developed to counter FTISC.
Motivated by this fact, a harvesting algorithm was proposed
that would manipulate the time rate of change of the control
law to eliminate the chattering phenomenon seen in Figure 3
and also avoid high-frequency oscillations that were pre-
sented in the previous study by McDonald [9]. To illustrate
this scenario, consider the FTISC phenomenon for harvest-
ing of the system, as given by Equation (1).

Example Three

This example illustrates the phenomenon of finite time
interval switching control. To illustrate the potential for
FTISC, let $\Delta = 0$ (perfect information); but rather than se-
lecting a harvesting effort, as in Equation (2), the derivative
of the control law is manipulated—see Equation (6):

$$\dot{u} = -\left(1/\epsilon_1\right)\sigma \qquad (6)$$

where, ϵ_1 is a small, positive parameter ($\epsilon_1 = 0.0001$).

As seen in Figure 4, this strategy from Equation (6) does
drive the biomass to expected levels, yet it is obvious that
the high-frequency oscillation is not appropriate for any
harvesting algorithm.
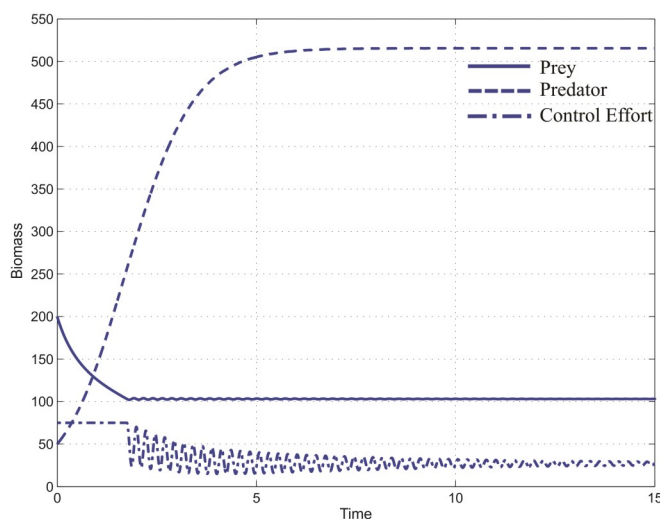
**Figure 4. Prey and Predator Biomass versus Time
(with harvesting effort FTISC)**

Continuous Time Harvesting Control

Consider the following: suppose that the time rate of
change of the control (harvesting) effort is manipulated, as
given by Equation (7):

$$\dot{u} = -\left[\left(\frac{1}{\epsilon_1}\sigma + \frac{1}{\epsilon_2}u\right)\right] \qquad (7)$$

which is termed continuous time harvesting control
(CTHC), and let ϵ_1, ϵ_2 be small, positive parameters.

If Equation (7) would cause the control effort to violate
the control bounds, then set $\dot{u} = 0$. The reasons for Equa-

tion (7) are as follows. Consider the term given in Equation (8):

$$\dot{u} = -\frac{1}{\epsilon_1}\sigma\ldots \tag{8}$$

Note that Equation (8) is analogous to Equation (6); if $\sigma < 0$, it would cause u to approach $u = u_{max}$; and, if $\sigma > 0$, it would cause u to approach $u = u_{min}$. Now consider the term in Equation (9):

$$\dot{u} = \ldots -\frac{1}{\epsilon_2}u \tag{9}$$

Note that Equation (9) introduces damping in that the time rate of change of the harvesting effort is the opposite of the sign of the harvesting effort u. This is the mechanism that allows for mitigation of FTISC. The utility of the combined strategy of Equation (7) can be validated by numerical simulation and its associated analysis.

Numerical Validation of CTHC

Consider the following examples that illustrate the efficacy of implementing CTHC for ratio-dependent predator-prey natural resource systems. The following four examples illustrate the behavior of CTHC in the absence of a disturbance.

Example Four

This example illustrates the utility of CTHC, Equation (7), given low initial levels of both predator and prey biomass. First consider the scenario where initial biomass of both predator and prey are equal to 50 in appropriate units with $\Delta = 0$. With the prey biomass level below that specified by $\sigma = 0$, set $u = u_{min}$. Also, let $\epsilon_1 = 0.0001$ and $\epsilon_2 = 0.1$. It is clear from Figure 5 that the optimization-based control algorithm CTHC very closely enforces $\sigma = 0$ in the steady state, where the steady values for prey and predator biomass are $x_1 = 103.49$ and $x_2 = 517.44$ in appropriate units, respectively.

Example Five

In this example the initial biomass of the prey and predator are each 50 in appropriate units and $\Delta = 0$. With the prey biomass level below that specified by $\sigma = 0$, set $u = u_{min}$. Also, let $\epsilon_1 = 0.0005$ and $\epsilon_2 = 0.1$. Figure 6 illustrates an immediate conclusion; the control (harvesting effort) exhibits virtually no initial oscillation. This is convenient in practice, sacrificing some accuracy, but the instantaneous switching or high-frequency oscillation of the harvesting

effort is eliminated. Observe that steady values for prey and predator biomass are $x_1 = 104.98$ and $x_2 = 524.89$ in appropriate units, respectively.

Figure 5. Prey and Predator Biomass versus Time (with harvesting effort)
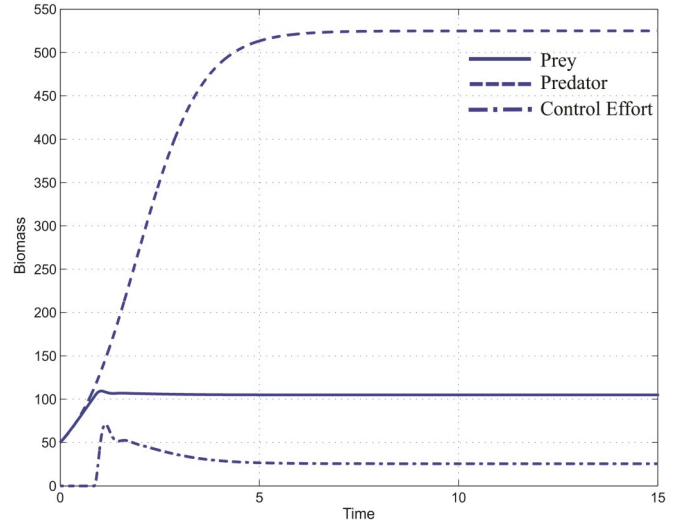
Figure 6. Prey and Predator Biomass versus Time (with harvesting effort and mitigation of FTISC)

Example Six

Consider the utility of CTHC, given high initial levels of prey and predator biomass levels of 200 in appropriate units and again let $\Delta = 0$. With the prey biomass level above that specified by $\sigma = 0$, set $u = u_{max}$. Now set $\epsilon_1 = 0.00025$ and $\epsilon_2 = 0.1$. It is clear from Figure 7 that some accuracy was

sacrificed, given that the steady values for prey and predator biomass are $x_1 = 104.06$ and $x_2 = 520.31$ in appropriate units, respectively.

Figure 7. Prey and Predator Biomass versus Time (with harvesting effort and slight loss of accuracy)

The following three examples illustrate the behavior of CTHC in the presence of a disturbance. This is meant for comparison purposes to behavior in the absence of a disturbance and to illustrate that undesirable behavior such as FTISC is mitigated. Simulation results in this subsection are presented and results are analyzed in the discussion section.

Example Seven

In this example, the utility of CTHC, given low initial levels of both predator and prey biomass, is demonstrated. Let the initial biomass of both predator and prey be equal to 50 in appropriate units. Now allow for a small disturbance in the prey dynamics, letting $\Delta = 0.1$. With the prey biomass level below that specified by $\sigma = 0$, set $u = u_{min}$ and let $\in_1 = 0.00025$ with $\in_2 = 0.1$. Once again, some accuracy has been sacrificed, as the steady values for prey and predator biomass are $x_1 = 104.07$ and $x_2 = 520.33$ in appropriate units, respectively. System behavior is illustrated in Figure 8. Again, consider varying initial conditions for the predator and prey biomass (and initial harvesting effort).

Example Eight

In this example, the utility of CTHC, given low initial levels of prey biomass, is demonstrated. Initial biomass of the prey is 50 in appropriate units and the predator biomass is 200 in appropriate units. Now allow for a small disturbance in the prey dynamics, letting $\Delta = 0.1$. With the prey

biomass level below that specified by $\sigma = 0$, set $u = u_{min}$ with $\in_1 = 0.00025$ and with $\in_2 = 0.1$. Once again, some accuracy has been sacrificed as steady values for prey and predator biomass are $x_1 = 104.07$ and $x2 = 520.33$ in appropriate units, respectively. This behavior is illustrated in Figure 9.
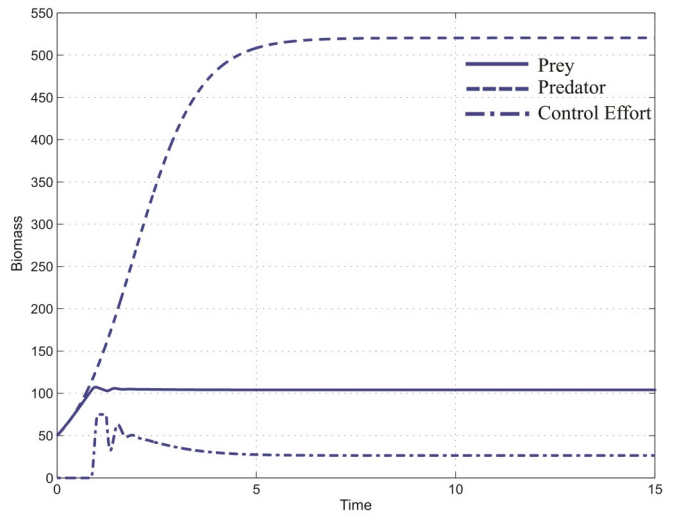
Figure 8. Prey and Predator Biomass versus Time (with harvesting effort and mitigation in the presence of a disturbance)
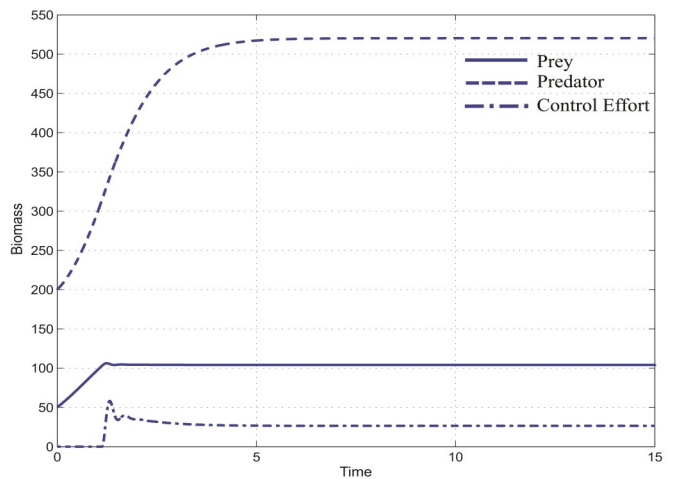
Figure 9. Prey and Predator Biomass versus Time (with harvesting effort)

Example Nine

Considered a scenario in which initial biomass of the prey is 50 in appropriate units and the predator biomass is 200 in appropriate units. Now allow for a large disturbance in the prey dynamics, letting $\Delta = 15.0$. With the prey biomass level above that specified by $\sigma = 0$, set $u = u_{min}$, with

$\in_1 = 0.00025$ and with $\in_2 = 0.1$. Once again, some accuracy has been sacrificed, given that steady values for prey and predator biomass are $x_1 = 104.58$ and $x_2 = 522.88$ in appropriate units, respectively. Figure 10 illustrates this behavior.

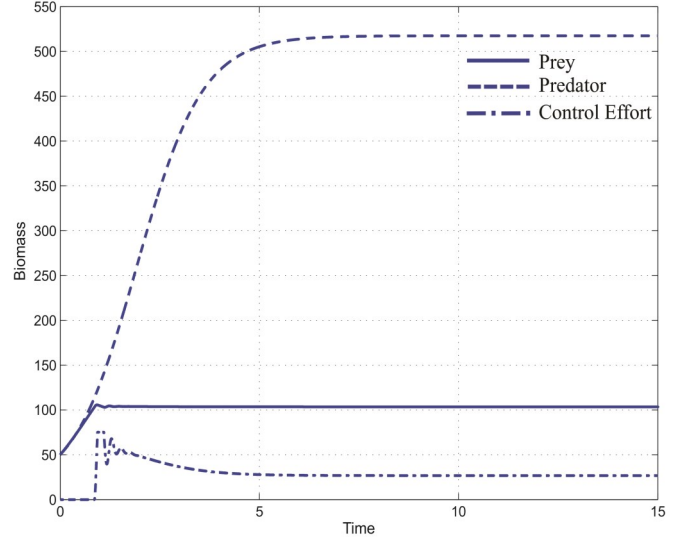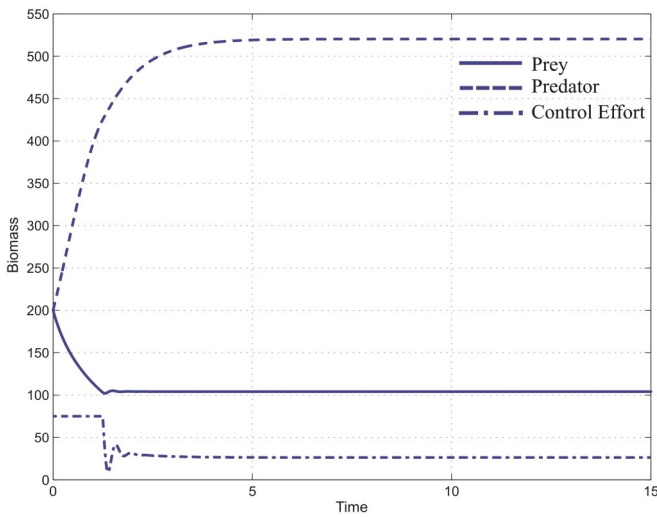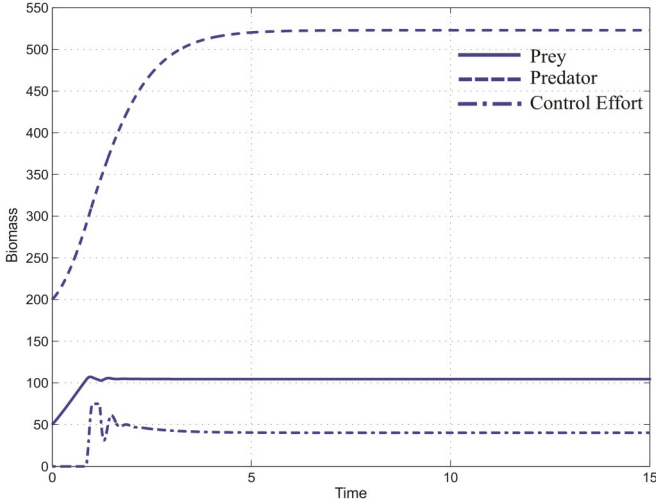**Figure 10. Prey and Predator Biomass versus Time (with harvesting effort)**

Discussion

Illustrative examples that demonstrate system behavior, from varying initial prey and predator biomass levels, with and without the presence of a disturbance, have been presented. Figure 1 illustrates the ratio-dependent predator-prey system behavior of Example One in the absence of harvest. This provides a baseline upon which the summarized IMNER algorithm performance may be illuminated. Example Two, via Figure 2, illustrated the utility of the IMNER algorithm with perfect prey biomass time rate of change information. Figure 3 illustrated how undesirable behavior in the form of instantaneous switching (chatter) of the harvesting (control) effort presents when a disturbance is introduced into the prey biomass time rate of change equation. Example Three via Figure 4 illustrated the FTISC phenomenon. While continuous, this high-frequency oscillation is not physically reasonable. In fact, such oscillation induced in mechanical systems has the potential to excite resonant modes.

Example Four via Figure 5 assumed perfect information ($\Delta = 0$) and invoked the CTHC algorithm Equation (7). A term within this algorithm that was negatively proportional to σ encouraged the prey biomass $x_1 \to x_1^*$, in effect satisfying $\sigma = 0$. This implicitly forces $x_2 \to x_2^*$. A second term, negatively proportional to the control effort u, tended to

discourage "overshoot" and the FTISC phenomenon. The examples illustrated the performance of CTHC from varying initial prey and predator biomass levels. Of particular interest is how well the algorithm performed in with a quite large disturbance $\Delta = 15.0$, which was detailed in Example Nine and Figure 10.

To quantify the benefits of CTHC, consider an error analysis for several scenarios. In Example Two, the IMNER algorithm generated steady values of prey and predator biomass, given perfect information. In Example Six, application of the CTHC algorithm resulted in differing steady values, but in the presence of a disturbance $\Delta = 0.1$. The percent error for this scenario for the prey biomass is given in Equation (10):

$$\left| \frac{103.09 - 104.06}{103.09} \right| \times 100\% = 0.94\% \tag{10}$$

and, for the predator biomass, is given in Equation (11):

$$\left| \frac{515.46 - 520.31}{515.46} \right| \times 100\% = 0.94\% \tag{11}$$

Now consider a worst-case scenario with Example Two, as the IMNER algorithm had access to perfection information. Compare this to Example Nine, where a large disturbance $\Delta = 15.0$ was present in the prey biomass time rate of change equation. The percent error for this scenario for the prey biomass is given in Equation (12):

$$\left| \frac{103.09 - 104.58}{103.09} \right| \times 100\% = 1.45\% \tag{12}$$

and, for the predator biomass, is given in Equation (13):

$$\left| \frac{515.46 - 522.88}{515.46} \right| \times 100\% = 1.44\% \tag{13}$$

These results are consistent with expectations as in the steady state; prey and predator biomass are related by $x_2 = vx_1$. Importantly, the percent error is quite small. In fact, the algorithm, given the considered disturbance, actually promotes preservation of the prey, as each of the biomass levels given the disturbance were larger in magnitude than in the case of perfect information. This is clearly illustrated by Equations (10)-(14). The totality of the numerical analyses confirms that the strategy of manipulating the time rate of change of the control effort avoids several parasitic behaviors. From these examples and associated simulations, the CTHC algorithm of Equation (8) clearly mitigates these unwanted behaviors and delivers a continuous and differentiable control law.

Conclusion

The fundamental point to be taken from this treatment is that continuous and differentiable control laws, achieved by manipulating the time rate of change of the control, can alleviate parasitic effects upon dynamic systems. In this case, a ratio-dependent predator-prey system was studied and an initial control law, IMNER, was invoked. This control law switched instantaneously across the surface defined by $\sigma = 0$. Example Two and Figure 3 illustrated the practical issues that make this harvesting effort impractical. To alleviate chatter, a continuous time alternative was proposed in Equation (6) and its behavior illuminated in several numerical simulations and associated figures. The phenomenon of FTISC is unwanted as well. Therefore, CTHC was proposed in Equation (8) and included terms, including the selected gain, that prompted enforcement of $\sigma = 0$ and terms (with gain) that "damped" the control effort. The utility of this in eliminating the undesired effects was shown in several examples, in the absence and presence of a disturbance, for a very small loss of accuracy.

References

 [1] McDonald, D. B. (2013). Locally Precise Response Surface Models for the Generalization of Controlled Dynamic Systems and Associated Performance Measures. *2013 ASME International Mechanical Engineering Congress and Exposition, 4*, 151-160. San Diego, CA, USA.

[2] McDonald, D. (2012). Instantaneous Optimal Control of a Predator-Prey Natural Resource with a Prey-Dependent Functional Response. *ASME Early Career Technical Journal*, *11*, 105-111.

[3] McDonald, D. (2014). Sensitivity Characteristics of Response Surface Models for Estimation of Ecological Parameters in Ratio-Dependent Predator-Prey Systems. *American International Journal of Contemporary Research*, *4*(6), 1-7.

[4] Goh, B. (1980). *Management and Analysis of Biological Populations, Developments in Agricultural and Managed-Forest Ecology 8*.

[5] Das, T., Mukherjee, R., & Chaudhuri, K. (2009). Bioeconomic Harvesting of a Predator-Prey System. *Journal of Biological Dynamics*, *3*(5), 447-462.

[6] Sun, G., Sarwardi, S., Pal, P., & Rahman, M. (2010). The Spatial Patterns through Diffusion-Driven Instability in Modified Leslie-Gower and Holling-Type II Predator-Prey Model. *Journal of Biological Systems*, *18*(3), 593-603.

[7] Froda, S., & Zahedi, A. (2009). The Spatial Patterns Simple Testing Procedures for the Holling Type II Model. *Theoretical Ecology*, *2*, 149-160.

[8] Kar, T., Pahari, U., & Chaudhuri, K. (2004). Management of a Prey-Predator Fishery Based on Continuous Fishing Effort. *Journal of Biological Systems*, *12*(3), 301-313.

[9] McDonald, D. (2013). Sensitivity Based Trajectory Following Control Damping Algorithms. *Numerical Algebra, Control, and Optimization*, *3*(1), 127-143.

Biography

DALE B. MCDONALD is an associate professor of mechanical engineering in the McCoy School of Engineering at Midwestern State University. He earned his BS, MS, and PhD degrees from Washington State University. Dr. McDonald's interests include the control of ecological systems, the radiographic sciences, optimal sedation, and collaborative art and STEM-inspired ceramics. Dr. McDonald may be reached at dale.mcdonald@mwsu.edu

DESIGN AND ANALYSIS OF A LABVIEW AND ARDUINO-BASED AUTOMATIC SOLAR TRACKING SYSTEM

Yuqiu You, Ohio University; Caiwen Ding, Syracuse University

Abstract

As solar energy system is becoming the major renewable system to replace conventional energy resources, the efficiency of such a system becomes an important factor for system implementation. Automatic solar tracking systems have been designed and studied by many researchers as the most practical method in efficiency improvement, but the high initial investment and low system efficiency still prevents wide implementation of this type of system. In this paper, the authors present a research project on design and analysis of an automated solar tracking system using LabVIEW and Arduino controllers. The system was designed and a prototype built with a solar panel, a stepper motor, a DC motor, motor drives, photosensitive sensors, LabVIEW system, and Arduino microcontroller. The mechanical design, hardware setup, component interfacing, software design, and circuit schematic were examined and demonstrated. The efficiency of the system is presented here by comparing it with a fixed solar system.

Introduction

Since an energy crisis is the most important issue in today's world, renewable energy resources are receiving priority to lessen the dependency on conventional resources. The solar energy system is becoming the major renewable system to replace conventional energy resources, due to the inexhaustible resource and its environmental advantages [1-3]. In a solar energy system, solar panels are used to directly convert solar radiation into electrical energy. Solar panels are made from semiconductor materials, which have a maximum efficiency of 24.5% in energy conversion [4, 5]. Unless a new material or technology is invented and applied in making solar panels, the most cost-effective method for improving the efficiency of solar panels is to increase the light intensity [6, 7]. A latitude tilt fixed PV system is still the major implementation for solar energy systems with low energy conversion efficiency, especially for small-scale household systems. Automatic solar tracking systems have been designed and studied by many researchers. However, most applied solar tracking systems are either too expensive on an industrial scale or small capacity at laboratory level with a shortcoming of high cost or low accuracy [8–18].

The purpose of this current research project was to design and implement an integrated control system with LabVIEW and Arduino in an automatic solar tracking system. A prototype of the system was designed and built with solar panels, a DC motor, a stepper motor, motor drives, photosensitive sensors, LabVIEW system, and Arduino microcontroller. The mechanical design, hardware setup, component interfacing, software design, and circuit wiring will be examined and demonstrated in this paper. The efficiency of the system is evaluated by comparing it with a fixed household solar system.

System Overview

The system design and construction contains two main parts, the hardware design and the software design and interfacing. The physical setup of the system includes the system frame, mechanical driver parts, photoelectric sensors, a DC motor, a stepper motor, and motor drivers. The software design and interfacing includes data acquisition, motion controls, and interfacing. Figure 1 shows the functional schematic diagram of the solar tracking system. There are four modules in the system architecture: photoelectric sensors anti-interference circuit, horizontal switch circuit, and vertical switch circuit, and horizontal vertical motor motion control. The horizontal switch circuit and the vertical switch circuits are controlled by the LabVIEW and Arduino-based controllers to implement the motion control on the DC motor and the stepper motor. Therefore, the system realizes the automatic tracking function. Figure 2 shows the 3D model of the system's physical setup is shown. The system was built with wood, a solar panel, 3D printed parts, and other mechanical and electronic parts.
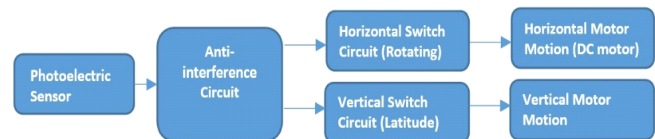
Figure 1. Schematic Diagram of the Solar Panel Tracking System

The solar panel could be sustained and elevated or declined through a connecting rod and a lead screw. The stepper motor

drove the translation screw or lead screw back and forth. Consequently, the lead screw nut was forced to move the connecting rod to elevate or decline the solar panel.
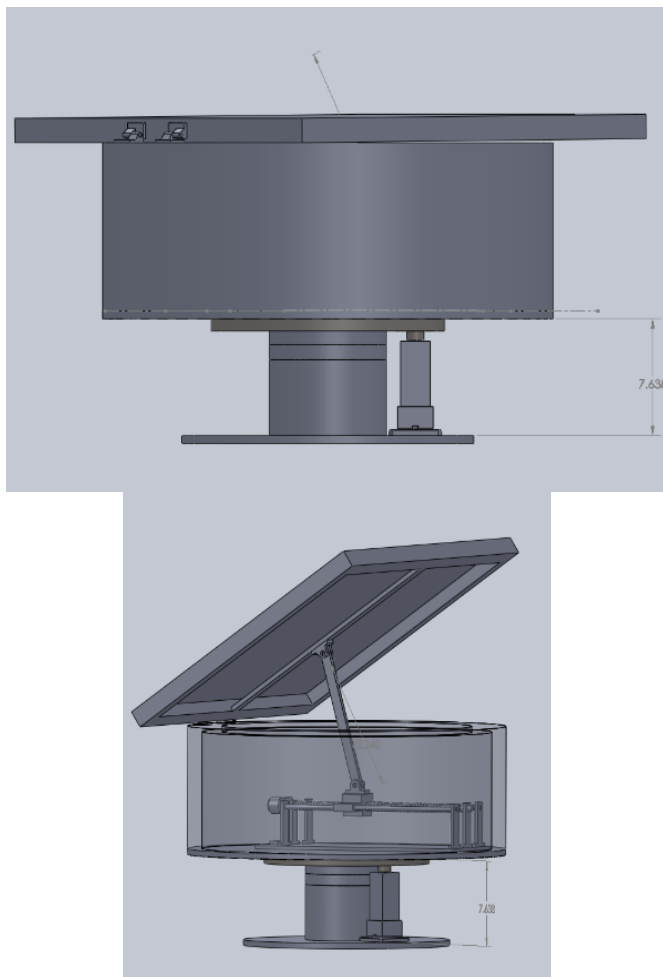
Figure 2. 3D Model of the Physical Setup of the System

As Figure 3 shows, the mechanical controller drives the solar panel up and down on latitude. The system base supports the solar panel system. The DC motor is attached to the base to control the horizontal rotation. Sun position varies based on different longitude, latitude, and time zone of the locations. The latitude motion controller assists with the horizontal rotation controller to realize the function of driving the solar panel focusing on the sun continuously. Figure 4 shows a lead screw nut is used as a linkage to connect the translation screw or lead screw with the connecting rod. The lead screw transfers the rotational motion to a linear motion. Figure 5 shows the horizontal (rotating) motion controller consists of a rotating frame and the supporting base with a pair of internal gears. The outer gear was attached to the rotating frame and the inner gear was attached to the stationary base.
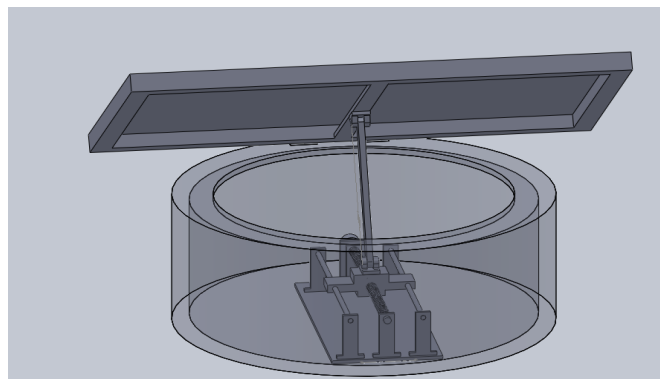
Figure 3. Latitude (vertical) Motion Controller
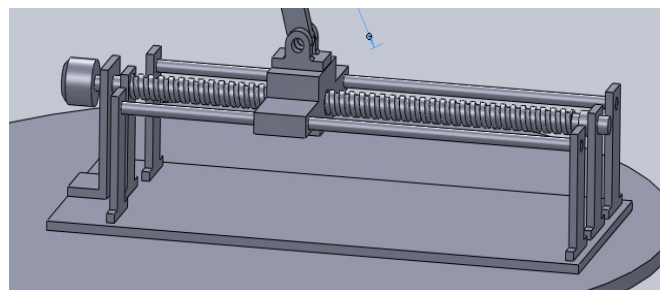
Figure 4. Translation Screw for the Latitude (vertical) Motion Controller

In the solar panel system, an inner gear is used for the DC motor to realize the horizontal motion [19, 20]. Inner gears are spur gears turned inside out. In other words, the teeth are cut into the inside diameter, while the outside diameter is kept smooth. This design allows for the DC motor to rotate the inner gear under the control of the LabVIEW and Arduino program to rotate the outer gear in further. The attached outer gear then rotates the frame. Figure 6 shows the completed system prototype. In Figure 7, a top view showing the detailed vertical motion control setup is provided.
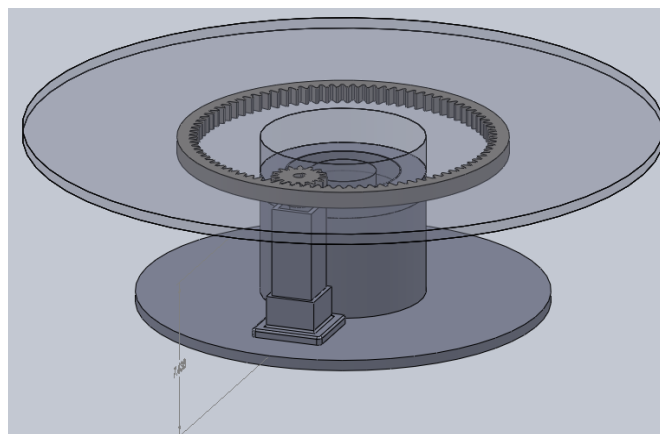
Figure 5. Horizontal (rotating) Motion Controller

Figure 6. System Prototype
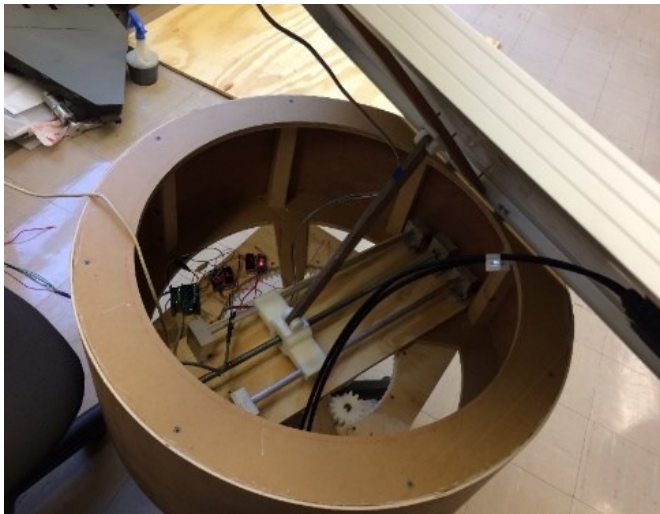
Figure 7. Vertical Motion Control Setup of the System

Software Design and Interfacing

In this current research project, software design and interfacing was based on the LabVIEW programming environment and consisted of data acquisition and Arduino motion control. LabVIEW is a development environment ideal for measurement and control systems with all of the tools that engineers and scientists need to build a wide range of applications. LabVIEW was used to provide an integrated interface for the whole system operation, and also the tool for data acquisition for the automatic solar tracker [21]. Arduino is an open-source microcontroller based on easy-to-use hardware and software. The Arduino Uno controller was programmed to provide motion control to the DC motor and the stepper motor, which, in turn, control the horizontal and vertical motion of the solar tracker.

The function of the data acquisition section is to acquire data from the photoelectric sensors [22]. A virtual instrument was built in LabVIEW for data acquisition from photoelectric sensors which integrates data detecting, signal modification, filtering, A/D processing, data acquisition, data logging, data processing, and data displaying together. Photoelectric sensors are normally made up of an LED, a receiver (phototransistors), a signal converter, and an amplifier. The phototransistor analyzes incoming light, verifies that it is from the LED, and appropriately triggers an output. When the photoelectric sensors detect sunshine, current flow will trigger an output for the photoelectric sensor. A data acquisition interface card (NI PCI-6229) and a connector board (NI SCB-68) were used to build the data acquisition channel between the LabVIEW software and the photoelectric sensors. Figures 8 and 9 show the interface and the LabVIEW program for the data acquisition section.
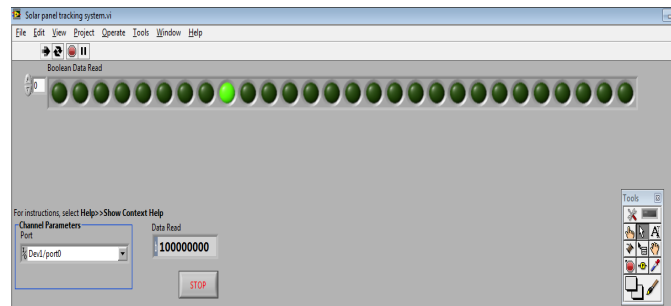
Figure 8. Data Acquisition Interface
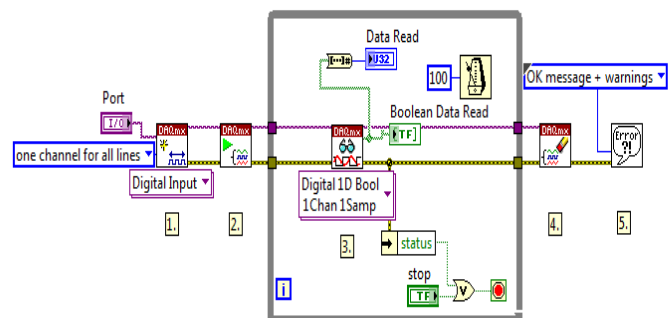
Figure 9. Data Acquisition Program

The motion control section of the solar tracker consists of horizontal and a vertical motion controls. Each motion control is realized through the control of a motor driver and a

motor. In this project, a DC motor was used with an L298N dual H-bridge DC motor driver for the horizontal motion, while a stepper motor with an EasyDriver stepper driver V4.4 was used for the vertical motion. The motion control section was integrated with the LabVIEW environment by using a LabVIEW interface for Arduino (LIFA) to acquire data from the Arduino microcontroller and process it in the LabVIEW environment. LIFA is used for connecting Arduino with Lab-VIEW to provide an interface controlling the EasyDriver stepper motor driver_v4.4 and the L298N dual H-bridge DC motor driver, thereby realizing control of the DC motor and the stepper motor. The LIFA realizes the control of the motors based on the data acquired from the photoelectric sensors through the LabVIEW environment. The control algorithm of the solar tracking system was designed according to the angle of the sun detected by photoelectric sensors. Figure 10 shows the wiring schematics of the DC motor driving system. The stepper motor driving system is similar to this one.
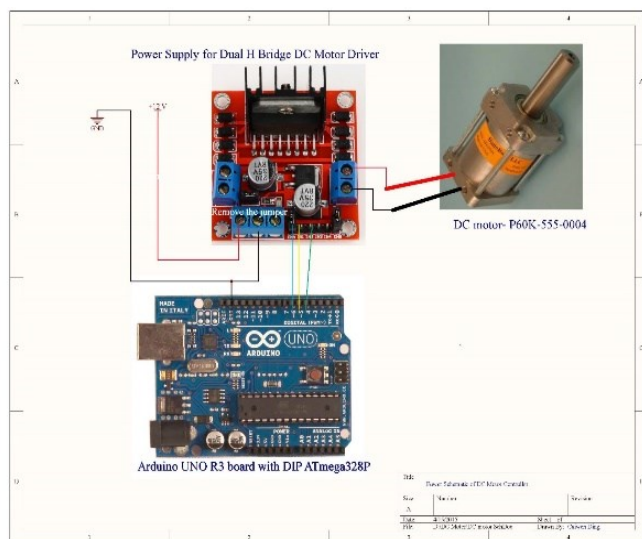
Figure 10. Wiring of the DC Motor Drive System

A closed-loop control system was used in the motion control of the automatic solar tracker. A closed-loop control system is also known as a feedback control system. Compared to an open-loop system, which has only a forward path, a closed-loop control system has one or more feedback paths, or loops, between its system input and output. Here, "feedback" means one or more branches of the system output return back to the system input to control the system itself [23]. Therefore, by monitoring the solar tracking system output and feeding back the system output to its input, the whole control system could be accurately controlled. The closed-loop control system was applied to automatically maintain the orientation of the solar panel to keep it facing the sun perpendicularly by comparing the desired solar panel position (orienting the sun upright continuously) with the actual orientation of the solar

panel. The implementation of the process generates an error signal that is the difference between the system desired input and system output. The error is determined by the status of the photoelectric sensors. The photoelectric sensors continually monitor the light intensity of the sun and feed a digital signal based on the corresponding light intensity of the sun back to the controller.

Also, the PID control method has been applied in the controller design. Because this required a high level of determinism and is vital to the consistent operation, the control loop typically closed on the board itself. Along with closing the control loop, the motion controller managed supervisory control by monitoring the limits and emergency stops to ensure safe operation. Directing each of these operations to occur on the board or in a real-time system ensures the high reliability, determinism, stability, and safety necessary to create a working motion control system. The LabVIEW interface for the overall automatic solar tracking system is shown in Figure 11. The interface contains all of the functional sections for the operation of the entire system: data acquisition, the stepper motor motion control (vertical motion), and the DC motor motion control (horizontal motion). The LabVIEW block diagram program of the software is shown in Figure 12.
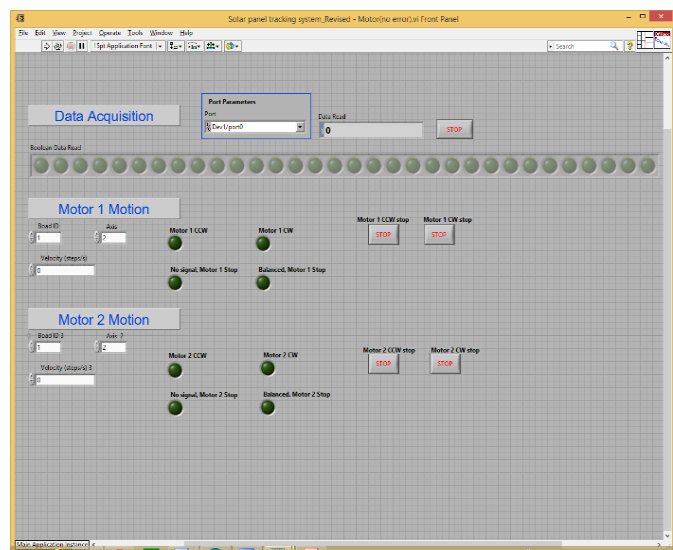
Figure 11. LabVIEW Interface of the Solar Tracking System

Findings and Conclusions

In order to verify that a solar tracking system produces more power over a longer time than a stationary array with the same number of modules, the energy conversion efficiency of a latitude-fixed PV system and an automatic solar tracking system were compared by using an energy consuming circuit, as shown in Figure 13.

Figure 12. LabVIEW Block Diagram Program of the Solar Tracking System

Figure 13. Energy Conversion Efficiency Testing Circuit

Equation (1) show the efficiency of energy devices can be defined as a quantitative expression between energy input and energy output. Equation (2) shows the energy conversion efficiency gain can be defined and calculated. For the energy device defined in this current research project, Figure 13 shows the useful energy output is the electrical power that can be calculated from the energy consuming circuit; the energy input is the solar energy that can be measured by using a solar meter. A Daystar's DS-05A solar meter was used for this project. In order to eliminate any possible disturbance from the light source during the data collection procedure, the experiment was conducted in an indoor laboratory using a sun simulator as the solar light source. The latitude angle of the sun simulator varied from 0° to 90° with an increment of 5° every five minutes. At each latitude angle, the output voltage

$$DeviceEfficiency(\eta) = \frac{usefulenergyoutput}{energyinput} = \frac{P}{E \times A_C} \tag{1}$$

$$Gain(\%) = \frac{MaximumEnergyoutput(Solartrac\,\mathrm{ker}) - Energyoutput(LatitudefixedPanel)}{Energyoutput(LatitudefixedPanel)} \tag{2}$$

Table 1. Data Measurement of the Output Voltage and the Output Current Based on the Fixed Panel

Simulator Angle/°	Output Current/mA			Output Voltage/V			Average Output Current/ mA	Average Output Voltage/V
90	198.00	198.50	200.00	2.03	2.03	2.03	198.833	2.030
85	192.60	193.30	195.00	2.03	2.03	2.03	193.633	2.030
80	186.20	186.20	188.00	2.03	2.03	2.03	186.800	2.030
75	178.50	179.20	180.70	2.03	2.02	2.02	179.467	2.023
70	170.80	170.00	172.70	2.02	2.01	2.02	171.167	2.017
65	160.70	161.00	164.20	2.02	2.01	2.02	161.967	2.017
60	150.00	152.00	154.00	2.03	2.01	2.02	152.000	2.020
55	140.70	142.50	142.80	2.02	2.00	2.02	142.000	2.013
50	130.70	132.30	131.90	2.02	2.00	2.01	131.633	2.010
45	120.90	121.40	120.90	2.03	2.00	2.01	121.067	2.013
40	109.40	108.90	109.90	2.03	1.99	2.01	109.400	2.010
35	97.60	99.00	98.00	2.03	1.98	2.00	98.200	2.003
30	85.50	86.20	86.80	2.02	1.97	1.98	86.167	1.990
25	73.70	75.50	76.60	2.02	1.96	1.99	75.267	1.990
20	63.50	65.30	65.10	2.01	1.98	1.99	64.633	1.993
15	54.20	54.40	54.10	1.99	1.97	1.98	54.233	1.980
10	39.70	43.60	43.50	1.98	1.95	1.97	42.267	1.967
5	31.70	35.00	34.90	1.96	1.94	1.95	33.867	1.950
0	29.10	30.30	30.50	1.95	1.93	1.93	29.967	1.937

and current were read from the energy consuming circuit from which the energy output was then calculated. Three data readings were conducted for each latitude angle of the sum simulator to eliminate any operating errors. Data were collected on a fixed solar panel (without the automatic control system) and on an automatic solar tracking system. The energy conversion efficiency and the efficiency gain of each system were calculated and compared. Table 1 shows the data collected based on a fixed solar panel.

Three group measurements were collected in the experiment and the data are displayed in the output current and the output voltage columns. In this project, the total solar cell size was calculated as 0.614 m². The input energy from the sun simulator is 35Watt/ m². The maximum efficiency occurred when the simulator's angle was 90°, and it could be calculated based on Equation (1) as 1.89%. The efficiency gain at this angle would be 600%, based on Equation (2). A fitted line plot was used to find the relationship between one predictor (the simulator's angle) and one response (the efficiency gain in %). The response variables are displayed on the y-axis and the predictor variables are displayed on the x-axis. A linear model was chosen to best describe the relationship between them. The relationship between the efficiency gain and the simulator's angle can be indicated by a mathematical expression: efficiency gain (%) = -0.4593 + 0.26656 latitude angle of the panel. Table 2 shows the calculated results. Even the maximum efficiency gain was as high as 600% for the fixed solar panel, but it only achieved this maximum gain for a short period of time when the sun simulator's angle was at 90°, which meant that the sun simulator was perpendicular to the fixed solar panel.

According to the data in Table 2, the output voltage and the output current at each latitude angle varied within a small range, due to the automatic solar tracking system's tracking function. The overall average of the output voltage can be calculated as 2.022 V and the overall average of the output current to be 190.218 mA. The energy conversion efficiency can be found by using Equation (1) and was determined to be 1.79% which is close to the maximum energy conversion efficiency of the fixed solar panel. Therefore, this experiment provides evidence that this automatic solar tracking system is able to keep the system energy conversion efficiency at the

Table 2. Data Measurement of the Output Voltage and the Output Current Based on the Automatic Solar Tracking System

Angle	Output Current/mA			Output Voltage/V			Average Output Current/ mA	Average Output Voltage/V
90	198	198	198.5	2.01	2.01	2.01	198.167	2.010
85	198	189	195	2.01	2.01	2.01	194.000	2.010
80	199	197	195	2.01	2.01	2.01	197.000	2.010
75	198	179.2	186	2.01	2.01	2.01	187.733	2.010
70	198	195	172.7	2.02	2.01	2.02	188.567	2.017
65	189	185	185	2.02	2.02	2.02	186.333	2.020
60	198	187	196	2.02	2.02	2.02	193.667	2.020
55	198	196	189	2.02	2.02	2.02	194.333	2.020
50	198	198	188	2.02	2.02	2.02	194.667	2.020
45	198	198	197	2.02	2.02	2.02	197.667	2.020
40	198	196	179	2.03	2.02	2.03	191.000	2.027
35	195	196	189	2.03	2.03	2.03	193.333	2.030
30	198	186	195	2.03	2.03	2.03	193.000	2.030
25	198	187	187	2.03	2.03	2.03	190.667	2.030
20	196	186	186	2.03	2.03	2.02	189.333	2.027
15	179	178	186	2.03	2.03	2.03	181.000	2.030
10	188	189	176	2.03	2.03	2.03	184.333	2.030
5	169	186	178	2.03	2.03	2.03	177.667	2.030
0	188	178	179	2.03	2.03	2.03	181.667	2.030

maximum valve during the latitude angle range from 0° to 90°. This also indicates that the controllers used in this tracking system are able to respond to the latitude angle changes in a timely way to keep the solar panel perpendicular to the sunlight.

In this study, the energy conversion efficiency of the solar panel was relatively low, compared to the maximum efficiency of 12% announced by the DOE. This could be explained by the fact that there are other factors that affect energy conversion efficiency, such as the temperature, the consuming circuit used, and the sun simulator. However, the automated solar tracking system is able to keep the energy conversion efficiency at the valve close to the maximum value achieved by the fixed panel at the latitude angle of 90°. The fixed panel can only momentarily get to this value. Thus, the solar tracking system enhanced the overall solar energy conversion efficiency. The energy conversion efficiency of the solar tracking system has been approved to determine the feasibility of a solar panel tracking system. The main reason to use a solar panel tracking system is to reduce the cost of the energy to some extent. A tracker produces more power than a stationary array or latitude tilt fixed PV system with the same number of modules. This additional energy conversion output, or "gain," can be quantified as a percentage of the output of the stationary array. The gain varies significantly with latitude and the orientation of a stationary installation in the same location. In general, a solar panel tracking system adds most to the output during the hours when a stationary array produces the least power.

This study could be a systematic foundation for future works to continue to build a solar panel system used either for household or industry. The DC motor and L298N dual H-bridge DC motor driver, the stepper motor, and the EasyDriver stepper motor driver V4.4 were tested and could be equipped on the solar tracking system to drive a solar panel with dimensions of 160 mm × 160 mm. As indicated in the tables and graphs, by applying a solar panel tracking system to a PV system, the energy conversion efficiency is increased significantly and is kept at the maximum level. The poor conversion efficiency associated with the latitude-fixed PV systems leads one to the conclusion that the development of a solar tracking system will be practical and significant. For future research, the energy conversion efficiency can be increased notably by applying an automatic solar tracking system to the PV system.

1. It is recommended that engineers and researchers develop more detailed experiments with a variety of motors and the corresponding drivers.
2. This current study provides a variety of designs for conducting research on a LabVIEW and Arduino-based solar panel tracking system. The structure of the solar panel tracking system is feasible. It is suggested that researchers could conduct comparisons with other structures and the structure that was used here.
3. It is suggested that researchers develop some type of experiments to study the system's energy dissipation through system friction and motor rotations.
4. It is also recommended that the test results could be

improved by conducting outdoor experiments under real sunlight instead of using a sun simulator. This requires more considerations in structure design and material selections.

References

[1] Alt, M. (2015). America's Top Solar Cities. Retrieved from http://www.huffingtonpost.com/margie-alt/americas-top-solar-cities_b_6979304.htm

[2] Early Solar History. (1999). Retrieved from http://solarcellcentral.com/history_page.htm

[3] Fox, C. (2014). The 20 Best Cities for Solar Power as America Prepares for an Energy 'Revolution' Retrieved http://www.huffingtonpost.com/2014/04/17/best-cities-solar-power_n_5162615.htm

[4] BP Statistical Review of World Energy 2014. (2014). Retrieved from http://www.commodities-now.com/reports/power-and-energy/16971-bp-statistical-review-of-world-energy-2014.htm

[5] History of Solar Energy in California - Go Solar California. (1999). Retrieved from http://www.gosolarcalifornia.ca.gov/about/gosolar/california.ph

[6] History of Solar Energy. (2012). Retrieved from http://exploringgreentechnology.com/solar-energy/history-of-solar-energy

[7] Horace de Saussure and his hot boxes of the 1700's. (2004). Retrieved from http://solarcooking.org/saussure.htm

[8] Lee, C. Y., Chou, P. C., Chiang, C. M., & Lin, C. F. (2009). Sun tracking systems: a review. *Sensors, 9*, 3875–3890.

[9] Lynn, P. (2010). *Electricity from sunlight: An introduction to photovoltaics*. Chicester: Wiley-Blackwell (an imprint of John Wiley & Sons).

[10] Maish, A. B. (1990). Performance of a self-aligning solar array tracking controller. *Proceedings of the IEEE Photovoltaic Specialists Conference*, Kissimmee, FL, USA.

[11] McFee, R. H. (1975). Power collection reduction by mirror surface non flatness and tracking error for a central receiver solar power system. *Applied Optics, 14*, 1493-1502.

[12] One Platform, Infinite Possibilities. (1999). Retrieved from http://www.ni.com/labview/why

[13] National energy strategy: Executive summary. (1991). Washington, D.C: U.S. Dept. of Energy.

[14] Semma, R. P., & Imamura, M. S. (1980). Sun tracking controller for multi-kW photovoltaic concentrator system. *Proceedings of the 3rd International Photovoltaic Sol Energy Conference*, Cannes, France.

[15] Sherwood, L. (2012). *U.S. Solar Market Trends 2011*. Interstate Renewable Energy Council (IREC) annual report.

[16] Smith, W. (1973). Effect of Light on Selenium during the Passage of an Electric Current. *Nature, 1*(173), 303-303.

[17] Trends in Photovoltaic Applications (2013). Retrieved from http://www.iea-vps.org/fileadmin/dam/public/report/statistics/FINAL_TRENDS_v1.02.pdf

[18] Zamostny, D. (2011). Solar history: Alexandre Edmond Becquerellar - Solar Energy World. Retrieved from http://www.solarenergyworld.com/2011/06/17/solar-history-alexandre-edmond-becquerel

[19] Dolara, A., Grimaccia, F., Leva, S., Mussetta, M.,Faranda, R., & Gualdoni, M. (2012). Performance Analysis of a Single-Axis Tracking PV System. *IEEE Journal of Photovoltaics, 2*(4), 524-531.

[20] Eke, R., & Senturk, A. (2012). Performance comparison of a double-axis sun tracking versus fixed PV system. *Solar Energy, 86*(9), 2665-2672.

[21] Building an NI Motion Control System. (2013). Retrieved from http://www.ni.com/white-paper/12127/en/

[22] Dunlop, J. (2010). *Photovoltaic systems*. (2nd Ed.). Orland Park, Ill.: American Technical.

[23] Fundamentals of Motion Control. (2014). Retrieved from http://www.ni.com/white-paper/3367/en/

Biographies

YUQIU YOU is an associate professor of engineering technology and management at Ohio University. She earned her BE degree from HuaZhong University of Science and Technology in China, MS degree from Morehead State University, and PhD (Technology Management, 2006) from Indiana State University. Dr. You is currently teaching at Ohio University. Her interests include computer-integrated manufacturing, automation control, and remote control systems. Dr. You may be reached at youy@ohio.edu

CAIWEN DING is currently a PhD candidate in the Department of Computer Engineering at Syracuse University. He earned his BE from Guangxi University in China and MS degree from Morehead State University. His research interests include automation control, power systems, and controller designs. Mr. Ding may be reached at cading@syr.edu

A Survey of State-of-the-Art Underwater Glider Technology: Development and Utilization of Underwater Gliders

Brian Johnson, Old Dominion University; Jennifer Grimsley Michaeli, Old Dominion University

Abstract

A subset of autonomous underwater vehicles (AUVs), referred to as autonomous underwater gliders (AUGs), is taking on an increasingly prominent role in long-endurance ocean research carried out by academia, military, and industry. Presently, the utilization focus of AUGs has a broad range, including ocean data acquisition, military surveillance, and others. The employment of gliders as a research tool is led by the need for a long-range, low energy consumption vessel. Similarly, the use of an underwater glider as a military asset is driven by the need for stealth undersea maneuverability and low energy consumption vessels. In this paper, the authors survey the technological variations, applications, and advancements of glider systems being employed by academic, military, and corporate research groups. In doing so, the connection between academic institution research with both military and commercial gliders is shown. Information of interest includes the type of gliders that have been developed over the past 30 years, the systems currently being developed, and future trends.

Introduction

Early ocean observation was limited to ship voyages. Although historical findings were made during these groundbreaking expeditions, such as the mid-Atlantic ridge and the Challenger Deep in the Mariana Trench, the compilation of results from their discoveries took far longer than the duration of the initial research cruise that gathered the data [1]. With further advancements in the technology used for oceanographic research, data could be compiled and analyzed at a much faster pace. Leading the advancement, the first profiling float, the autonomous Lagrangian circulation explorer (ALACE) was able to alter its buoyancy to sample vertical columns of the ocean [2]. The coupling of this buoyancy control and wings would allow for the generation of lift. With horizontal flight derived from a change in buoyancy, the autonomous underwater glider was created.

In order to broaden public knowledge of AUGs, both commercially available gliders and the models currently in development are discussed. The compilation of research conducted in this field of study will facilitate researchers interested in the scientific topic discussed. As an additional service, the survey will instruct where supplemental information on the topic can be found.

First-Generation, Buoyancy-Driven Gliders

Slocum Electric

Having learned from the previous development of ALACE's buoyancy system, the Slocum Electric glider was the first system to realize controlled horizontal motion. While in its horizontal flight orientation, the Slocum Electric glider was able to alter heading with an active rudder system, allowing for quick reaction and increased maneuverability in shallow waters. The Slocum Electric glider was also equipped with a CTD sensor used to measure conductivity, temperature, and depth. The Slocum Electric glider design is one that contemporaries have used as a model to create designs of their own. With an ellipsoidal aluminum 6061-T6 hull, the Slocum Electric was able to reach depths of 200 meters for a range of 4600 km over 200 days [3]. Due to the shallow operating depth, the glider used a more robust single-stroke pump [2].

Slocum Thermal

The Slocum Thermal glider utilizes environmental energy to move through the ocean waters. Changes in the vessel's buoyancy allow for vertical motion which, when coupled with fixed wings, provides the necessary dynamic forces to transverse horizontally as well. Capitalizing on the ocean's temperature gradients for buoyancy manipulation allows the thermal glider's batteries to function primarily as the power source for onboard equipment. The conservation of power using the thermal buoyancy system results in gliders with extended mission durations when compared to electric counterparts. The Slocum Thermal has a length of 1.5 m, a hull diameter of 21.3 cm, and weighs 60 kg. It can reach a maximum depth of 1200 m. Due to the alternate approach in buoyancy control, the design differs from that of the electric version, most notably by the need for longitudinal underbody tubes used for storage and movement of the working

fluid. The thermal buoyancy system operates through the volumetric changes experienced by the working fluid as the glider travels through the thermocline present in the ocean [4]. Although the technology allows the vessel to achieve a range of 40,000 km at 0.4 m/s over a five-year period of autonomous ocean observation, the energy efficiency is estimated to be as low as 3% and can only be utilized in 65% of the world's oceans, due to its dependence upon adequate ocean temperature gradients [3, 4]. Further motion control is realized similar to that of the electric version's battery pack movement [3, 5].

Seaglider

More than any other glider in its class, the Seaglider's capabilities are a result of its advanced internal and external design. Made to operate at much greater depths than the Slocum Electric, the Seaglider controls its buoyancy with a multi-stroke pump [2]. The length of the hull and shroud is 180 cm with an overall length of 330 cm. The diameter is 30 cm and the vessel weighs 52 kg, with a 4 kg allocation for payload. Although the internal operations of its actuators are very similar to that of other electric gliders, the Seaglider's external design is where its advantages are fully realized.

External development of the Seaglider's hydrodynamic design was carried out by R. M. Hubbard and the research conducted at the University of Washington—Applied Physics Laboratory. The vessel's configuration is composed of a pressure hull, located internally, and an external fiberglass fairing hull [6]. The design of the external hull follows that of the University of Washington—Applied Physics Laboratory's (UW/APL) wind tunnel-tested AEMT vehicle, resulting in a modified glider hull that can sustain "laminar flow over more than 80% of its surface" [6]. The streamlined shape of the Seaglider results in reduced drag and equates to substantial energy conservation and increased endurance. The Seaglider has a range of 4600 km and an endurance of 200 days.

Spray

In collaboration with the Webb Research Corporation (WRC), the design of the Spray consists of a single hull that also acts as the vessel's pressure hull. The hull is 200 cm in length, 20 cm in diameter, and carries 2.5 kg of payload for its full load of 51 kg. The divergence from the two-hull method of the Seaglider provided a design variation within the Autonomous Ocean Sampling Network program and commenced after the utilization of data collected from both the Slocum and Seaglider [7]. Through experimental testing of multiple hull forms, and the continued support from Doug Webb of WRC and Erikson from UW/APL, the Spray

hull form was optimized for improved performance. Compared to the two electric gliders developed previously, specifically the Slocum Electric and the Seaglider, the Spray hull outperformed both of these gliders with the lowest drag measurements across the range of Reynolds numbers [7].

Final design choices required internal additions and alterations. Due to the deep ocean depths encountered during utilization, the hull was stiffened internally through strategically placed internal rings/hoops [7]. Similar to the development of the Slocum Electric glider, elements from the ALACE design were applied to the internal design of the Spray hull. During development, problems with the hydraulic system, taken from ALACE, were solved with "a different SIO design with a compression ratio greater than 3:1…" [7]. The Spray has a range of 7000 km and an endurance of 330 days. Communication from the glider was made possible through a transceiver located within the wing. The location of the transceiver requires that the glider perform a 90 degree roll in order to allow for the antennae to achieve the greatest height above the surface of the ocean.

Novel Types of Gliders

The Solar Type: SORA

In 2010 and 2011, researchers at the Osaka Prefecture University published the progress of their work regarding the feasibility of a solar-powered underwater glider. Motivated to utilize environmental energy for power, the researchers proposed a method for improving the glider's long-term endurance. In need of a research test-bed, development of the SORA glider commenced. Unlike the first generation of buoyancy-driven gliders, the SORA glider was equipped with two forward-positioned thrusters for flight control. The decision for thruster integration was chosen over typical buoyancy systems in order to reduce overall vehicle complexity. The thrusters were solely powered from amorphous-silicon solar panels [8]. The solar cell's ability to capture the available blue-color wavelength, while still immersed, provided the most efficient power supply. Figure 1 shows the solar panels were located over the top surface of the glider.

Testing commenced at the Ocean Engineering Tank of the Research Institute for Applied Mechanics (RIAM), Kyushu University in Fukuoka, Japan, on March 19, 2010 [8]. The operation starts following capacitor charging from the solar cells. The charge from the capacitor is then supplied to the thrusters in order to initiate the dive sequence. When sunlight is no longer attainable, the thrusters stop and the glider begins to resurface. Figure 2 depicts the glide path.

Figure 1. Solar-Powered Underwater Glider, SORA
Note. From "Development of a Solar-Powered Underwater Glider," by M. Arima, T. Okashima, and T. Yamada, 2011, *Proceedings, IEEE Symposium on Scientific Use of Submarine Cables and Related Technologies*, pp. 1-5. Reprinted with permission.
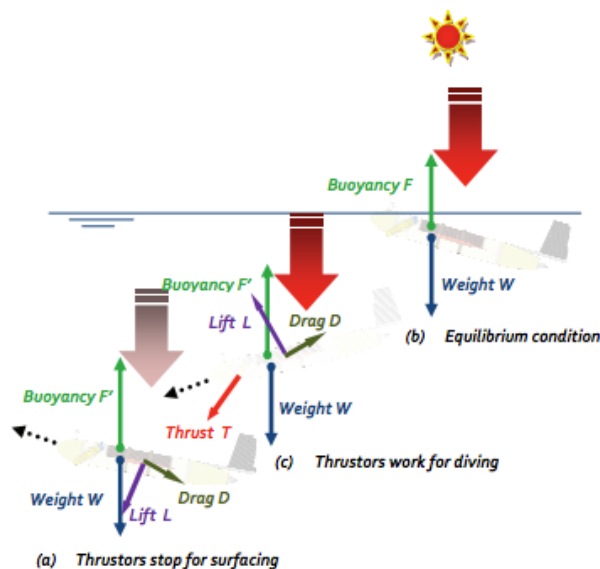
Figure 2. SORA Glide Procedure
Note. From "Development of a Solar-Powered Underwater Glider," by M. Arima, T. Okashima, and T. Yamada, 2011, *Proceedings, IEEE Symposium on Scientific Use of Submarine Cables and Related Technologies*, pp. 1-5. Reprinted with permission.

The glide test failed, due to the use of fluorescent lights and incandescent lamps instead of natural sunlight. Although light intensity within the indoor facility was inadequate for optimal performance, "the relationship between the light intensity, depth, and capacitor voltage" was ob-

tained [8]. Validation of the novel design allowed for further research to be conducted for realization of an ocean-going, solar-powered underwater glider.

Tonai60

In 2014, Osaka Prefecture University presented the ocean-going, solar-powered underwater glider named Tonai60. Figure 3 shows the glider's hybrid solar panels cover a 1.65 meter by 1.03 meter area and have a cylindrically shaped hull attached below the solar panels. In support of Japan's Ministry of the Environment, the solar-powered underwater glider acts as a system for coral monitoring [9]. Due to the innate sensitivity of reef corals, the marine invertebrates provide a natural means of notification of ocean environment changes. In need of a method of observation not hindered by human or remote technology limitations, Tonai60 and its suite of sensors were developed.
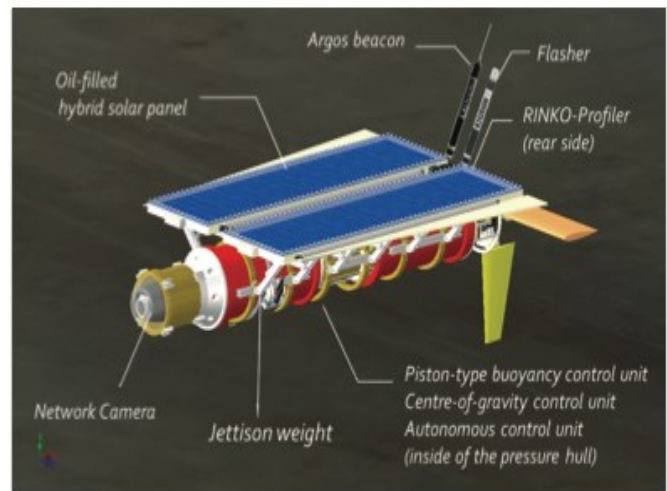
Figure 3. External View of the Tonai60 Glider
Note. From "Development of a Coral Monitoring System for the Use of Underwater Vehicle," by M. Arima, K. Yoshida, and H. Tonai, 2014, *Proceedings in OCEANS 2014 – TAIPEI*, pp. 1-6. Reprinted with permission.

Designed to monitor the Twilight Zone, more commonly known as the Disphotic Zone, the vessel is able to reach depths of 60 meters. The glider's RINKO-Profiler is able to take temperature, conductivity, salinity, dissolved oxygen, chlorophyll, and turbidity measurements at varying depths, all of which are closely related to the health of the coral. In addition to the sensors, Tonai60 is equipped with a high-sensitivity network camera. The VB-M40 network camera is the key to operations in dark conditions. Following excitation of coral fluorescence, images are taken. The camera is located at the forward section of the glider hull to capture images similar to those depicted in Figure 4.
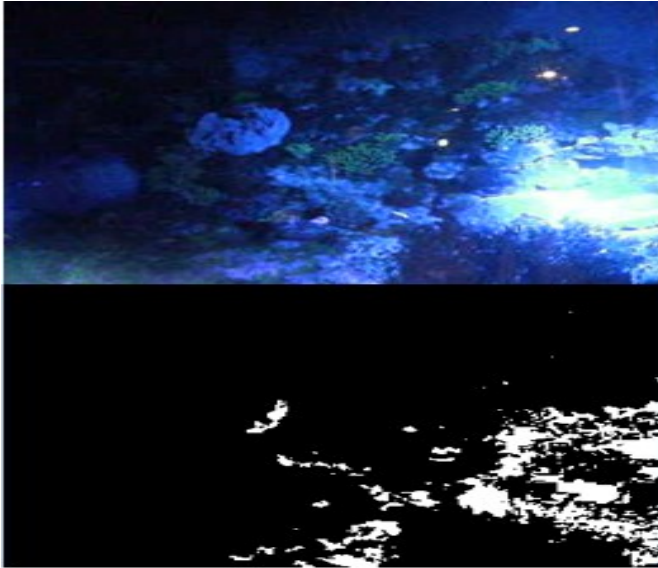
Figure 4. Ultraviolet Light Image (top) and Binary Image (bottom)
Note. From "Development of a Coral Monitoring System for the Use of Underwater Vehicle," by M. Arima, K. Yoshida, and H. Tonai, 2014, *Proceedings in OCEANS 2014 – TAIPEI*, pp. 1-6. Reprinted with permission.

Tank tests were conducted at the Coral Tank of Enoshima Aquarium, Fujisawa, and Kanagawa [9]. During manual simulation, the monitoring system proved to be effective at capturing both color and binary images of coral [9]. Sea trials at Kagoshima Bay are to be followed by further field experiments to achieve better view control and image quality [9].

The Flying Wing

Researchers at the State Key Laboratory of Autonomous Underwater Vehicles, located in China, are investigating a means of increasing underwater glider's glide efficiency. In order to conduct tests and solve the efficiency problem at hand, a flying wing underwater glider, simply titled HFWUG, was developed. In 2015, their methods and results were published. The first study required computational fluid dynamic (CFD) simulation. Software for this process included Solid Works for 3D modeling, GAMBIT for grid topology and boundary conditions, and FLUENT as the flow solver [10]. Validation of the CFD model required calculation of hydrodynamic forces for a trapezoidal hydrofoil with available experimental data. Comparison of the experimental lift and drag forces to that of the simulation showed acceptable trend error [10]. A flying wing design with a 1.2-meter chord length and geometric aspects similar to that of a NACA66-023 airfoil was found to have the maximum lift-to-drag ratio. The high ratio mentioned will result

in an increased horizontal glide distance traveled per unit traveled in the vertical direction [10]. "The HFWUG has a wing span of three meters, an aspect ratio of five to eight, and expected velocity of 1 knot to 3 knots" [10].

The hulls of conventional gliders produce little lift. The final lift-to-drag ratio of HFWUG was found to be nearly three times greater than conventional gliders, such as the Slocum, Seaglider, and Spray. HFWUG is used as an investigation model, whose results can be used to help make other underwater gliders more efficient during underwater flight. In the future, the effects of different appendages, such as winglets and flaps, will be evaluated [10].

Applications

Commercial

All of these first-generation gliders mentioned transitioned to commercially available products. With continued innovation, they remain leaders in the market. Due to the vast number of gliders that exist, this section focuses upon the continued leader of the underwater glider market, the Slocum glider. The spectrum of AUVs available can be found through the Autonomous Undersea Vehicle Applications Center (AUVAC) database [5]. Even within the Slocum family of gliders, there are physical variations. In addition, the underwater glider's functions range from environmental survey to submarine surveillance. Hand-in-hand with the range of applications is the variation of mechanical and electrical systems and devices necessary for the vessels to perform their designated missions.

Military

Teledyne Webb Research has delivered nearly 500 Slocum gliders around the world [11]. The gliders play a major role in both the Navy Littoral Battlespace Sensing program and the Ocean Observatories Initiative program [11]. As the leading provider of commercial gliders, Teledyne secured a contract with the United States Navy worth an estimated $52.6 million. The gliders will "support the Navy's littoral and deep-water missions" [12].

Hybrid

Hybrid gliders are able to complete missions that require greater maneuverability. The Slocum G2's increased efficiency is a result of the integration of foldable propeller blades, which results in decreased drag effects as the propeller retracts when not in operation. In conjunction with the foldable propeller blades, Slocum G2's neutral buoyancy

mode during horizontal propulsion allows the vessel to conserve energy by not having to expend additional power to maintain a desired depth [11]. Previously, buoyancy-driven gliders were required to drift after encountering a strong current. Now, hybrid gliders possess the speed necessary to overcome strong eddies in a more efficient manner than had been seen a decade ago. Through technological enhancements, hybrid gliders remain more efficient in adverse conditions than typical gliders on the market.

Storm

Slocum glider's ability to operate in adverse conditions makes it highly suitable for storm data collection. Currently, the measure most in need of improvement is storm intensity. Recent incidents of fallacy include the intensity overprediction of Hurricane Irene in 2011 and the intensity under-prediction of Hurricane Sandy in 2012. "Inaccuracies in intensity, in either direction, present issues with preparedness levels, public trust, and resource alignment" [11]. The two storms' combined damages are estimated at $75 billion. Storm gliders, in combination with both satellite ocean color and sea surface temperature, could decrease such inaccuracies in the future [11].

Education

The foundation for underwater glider design and development is being built at universities across the world. Students and faculty are creating their own gliders at their respective universities of study and work. Considering the cost of current commercially available vehicles, undergraduates and graduates are opting to build their own vessels for student research purposes.

ROGUE

For a number of years, the ROGUE laboratory glider continued to be used as an experimentation platform for glider dynamics and control at Princeton University. The small glider's 18"-by-12"-by-6" ellipsoidal-hull shape housed four internal ballast tanks for pitch and roll actuation [13]. Modularity of external wings and tail allowed for variation during hydrodynamic evaluations from the model's standard tail volume and 28-inch wing length. Designed from ultra-high molecular weight plastic, models were made to fit and be fully tested within Princeton's laboratory tank and pool. The ease of model modification provides a way to investigate the stabilization of glide paths with differing vehicle parameters. Results, and the principles discovered from such models, are then expanded for implementation on multiple gliders at once [14].

Bumblebee

During 2011 and 2012, students at the Florida Institute of Technology built an underwater glider for education and research called Bumblebee. Bumblebee's design is based on the research of Cheryl Skibski and Alexandra Gottschall. Originally created as a graduate-level proof-of-concept for the use of external control surfaces on a glider, the research continued and advanced through the efforts of undergraduates at the institute [15]. Bumblebee is a buoyancy-driven glider that weighs less than 25 kg and measures 2 meters in length [15]. The vessel is able to reach depths of 100 meters through a custom-built piston-type buoyancy engine and a 6061-T6-aluminum alloy pressure housing [15]. The vessel's pressure housing is surrounded by a fiberglass fairing to which wings are attached. The NACA 65010 airfoil-shaped external wings being investigated act as the primary means for vehicle steering [15].

The outer housing has a teardrop shape. Ballast weights and foam are added to the internal fairing, depending upon the density of the fluid in which the vessel is required to maneuver. The Bumblebee glider uses the Overo Fire computer-on-module by Gumstix for its main control system, which includes controls of the buoyancy engine and the wing flap servos [15]. The glider typically operates on short missions lasting two and a half days and requires five 6V lead-acid batteries. The vessel would require lithium-ion batteries in order to achieve week-long research durations [15]. User communication during missions is transmitted to remote computers via RF [15].

GUPPIE

In 2013, research was published regarding the work on a Glider for Underwater Problem-Solving and Presentation in Education (GUPPIE). The educational vessel was developed in Michigan Technological University's Nonlinear and Autonomous Systems Laboratory (NAS Lab) as a platform to facilitate STEM learning [16]. The small-sized, lightweight, and inexpensive glider serves as a hands-on learning platform for glider mechanics and mechatronics. GUPPIE is composed of three materials: PVC (polyvinylchloride), acrylic, and aluminum. The materials for GUPPIE were chosen for their low cost and machinability. In addition, the transparency of the acrylic material facilitates learning of the internal mechanisms at work within the hull. The modular, reconfigurable design of the GUPPIE allows for the integration of more complex components, as the student learns more advanced STEM concepts.

As a buoyancy-driven vessel, the glider implements syringes for internal hydraulic accumulation. Full actuation of

the syringes results in a nearly 45 degree dive path [16]. In order to add control, and to make efficient use of the syringe's ballast-altering capabilities, the hydrodynamic surfaces include a vertical stabilizer and high aspect ratio wings [16]. The electrical system is controlled through an Arduino Uno. The open source hardware and software, associated with Arduino products, allows students to make alterations at a much faster pace. The electrical system is powered by a lithium-ion battery pack, which provides 30 minutes of operation [16].

Education gliders have expanded from laboratory research tools to undergraduate and graduate thesis concentrations. They are now being used to bridge the gap between college and high school students, as cheaper means of construction are realized. The gliders continue to serve as a multidisciplinary endeavor, as their design requires the knowledge of multiple fields of engineering and computer science. New gliders continue to be developed, as universities strive to make footprints of their own.

Military

In 2007, the Office of Naval Research formed the Passive Acoustic Autonomous Monitoring (PAAM) of Marine Mammals program. "Focused on passive acoustic systems for autonomous detection, classification, localization, and tracking of marine mammals," the program aids in monitoring Navy exercise areas [17]. The Navy's interest in the Liberdade Flying Wing Glider program's XRay vehicle led to the development of the next generation of flying wing gliders. Part of the PAAM system, the ZRay buoyancy-driven underwater glider was developed as a test platform for real-time underwater detection [17]. It should be noted that acoustic sensor systems are used in both anti-submarine warfare and mine-countermeasure systems [18]. Similar to the XRay glider, the ZRay glider was given a large flying wing design. The massive task was accomplished through the combined efforts of the Marine Physical Laboratory, Scripps Institution of Oceanography and Applied Physics Laboratory, and the University of Washington [17]. Their efforts provided a vessel with a 20-foot wingspan and high lift-to-drag ratio, resulting in increased glide efficiency when monitoring.

Future Trends

Review of current literature indicates that the development of the next generation of gliders will likely include increased trending towards hybridization. An increasing number of commercially available gliders have installed propellers or an alternate propeller-driven model. On a

smaller scale, there is also research being conducted that will allow for gliders to transition into remote operated mode when in shallow waters, such as the case with the SOARER glider in Japan [19]. Multi-glider missions will also likely continue to be a focal point. Although the current state-of-the-art gliders differ in design, many are intended to work in groups to fulfill a specific purpose or mission [1, 2, 4-6, 11, 14, 18, 20].

In order for either hybridization or multi-glider coordinated missions to reach their full potential, systems must become more advanced. Technology advances to achieve greater vessel efficiency, both in terms of vessel design towards drag reduction as well as more optimal power management strategies, will continue in response to the persistent demand for longer-endurance gliders. In parallel, the authors of this current study anticipate a greater emphasis on control system design, functionality, redundancy, and interface protocols. Such advances in control systems will allow operators to achieve robust health monitoring and near, real-time glider management, and enhanced maneuverability [11]. Over the years, more notable than the change in the configuration of gliders is the diverse type of payloads and equipment that need to be integrated. Therefore, it is not clear what project will yield the next Slocum, Seaglider, or Spray; it is only definite that, as underwater technology advances, gliders will continue to increase in number, application, and endurance.

Conclusions

In this paper, the authors presented a survey of technological variations, applications, and advancements of autonomous underwater glider systems being employed by academic, military, and corporate research groups. Information of interest includes the type of gliders that have been developed over the past 30 years, the systems currently being developed, and future trends.

Acknowledgments

References

[1]   Bachmayer, R., Leonard, N. E., Graver, J., Fiorelli, E., Bhatta, P., & Paley, D. (2004). Underwater Gliders: Recent Developments and Future Applications.

Proceedings, International Symposium on Underwater Technology, (pp.195-200).

[2] Rudnick, D. L., Davis, R. E., Eriksen, C. C., Fratantoni, D. M., & Perry, M. J. (2004). Underwater Gliders for Ocean Research. *Marine Technology Society Journal*, 38(1), 48-59.

[3] Skibski, C. E. (2009). Design of an Autonomous Underwater Glider focusing on External Wing Control Surfaces and Sensor Integration.)Master's thesis). Retrieved from: http://my.fit.edu/~swood/GliderThesisFinal.pdf

[4] Webb, C., Simonetti, P. J., &Jones ,C. P. .(2001) SLOCUM: An Underwater Glider Propelled by Environmental Energy. *IEEE Journal of Oceanic Engineering, 26*(4), 447-452.

[5] Barker, W. P. (2012). An Analysis of Undersea Glider Architectures and an Assessment of Undersea Glider Integration into Undersea Applications. (Master's Thesis). Retrieved from http://calhoun.nps.edu/handle/10945/17320.

[6] Eriksen, C. C., Osse, T. J., Light, R. D., Wen, T., Lehman, T. W., Sabin, P. L., et al. (2001). Seaglider: A Long-Range Autonomous Underwater Vehicle for Oceanographic Research. *IEEE Journal of Oceanic Engineering, 26*(4), 424-436.

[7] Sherman, J., Davis, R. E., Owens, W. B., &Valdes , J. (2001). The Autonomous Underwater Glider Spray. *IEEE Journal of Oceanic Engineering, 26*(4), 437-446.

[8] Arima, M., Okashima, T., &Yamada, T. (2011). Development of a Solar-Powered Underwater Glider. *Proceedings*, *IEEE Symposium on Scientific Use of Submarine Cables and Related Technologies*, (pp.1-5).

[9] Arima, M., Yoshida, K., & Tonai, H. (2014). Development of a Coral Monitoring System for the Use of Underwater Vehicle. *Proceedings in OCEANS 2014 – TAIPEI*, (pp.1-6).

[10] Zihao, W., Ye, L., Aobo, W., & Xiaobing, W. (2015). Flying Wing Underwater Glider: Design, Analysis, and Performance Prediction. *Proceedings, International Conference on Control, Automation and Robotics (ICCAR)*, (pp.74-77).

[11] Jones, C., Allsup, B., & DeCollibus, C. (2014). Slocum glider: Expanding our Understanding of the Oceans. *Proceedings, Oceans*, (pp.1-10).

[12] Teledyne Wins $6.2M U.S. Navy Glider Contract. (2009, March 23). *Teledyne Technologies' Everywhereyoulook*. Retrieved from http://teledyne.com/news/tdy_03232009.asp.

[13] Graver, J. G. (2005). *Underwater Gliders: Dynamics, Control and Design.* (PhD Thesis). Retrieved from https://www.princeton.edu/~naomi/theses/jgggraver-thesis-4-11-05.pdf.

[14] Bhatta, P., & Leonard, N. E., (2002). Stabilization and coordination of underwater gliders. *Proceedings, IEEE Conference on Decision and Control*, (pp.2081-2086).

[15] Gottschall, A. K. (2012). Design of an Underwater Glider for Education and Research. *Proceedings, IEEE Conference on Autonomous Underwater Vehicles*, (pp.1-4).

[16] Mitchell, B., Wilkening, E., &Mahmoudian, N. (2013). Developing an Underwater Glider for Educational Purposes. *Proceedings, IEEE International Conference on Robotics and Automation (ICRA)*, (pp.3423-3428).

[17] D'Spain, G. (2011). Follow-On Tests of the ZRay Flying Wing Underwater Glider and Waveglider Autonomous Surface Vehicles, and their Passive Acoustic Marine Mammal Monitoring Systems. *Final Report of the Passive Autonomous Acoustic Monitoring of Marine Mammals Program*, (pp. 1-22).

[18] Rogers, E. O., Genderson J. G., Smith, W. S., Denny, G. F., & Farley, P. J. (2004). Underwater Acoustic Glider. *Proceedings, IEEE International Geoscience and Remote Sensing Symposium (IGARSS)*, (pp.2241-2244).

[19] Arima, M., Tonai, H., & Kosuga, Y. (2013). Underwater Glider 'SOARER' for Ocean Environmental Monitoring. *Proceedings, IEEE International Underwater Technology Symposium (UT)*, (pp.1-5).

[20] Reed, B., Ambler ,C., Guerrero, J., &Hover ,F. (20-11). Vertical Glider Robots for Subsea Equipment Delivery. *Proceedings, IEEE International Conference on Robotics and Automation (ICRA)*, (pp.2356-2361).

Biographies

BRIAN JOHNSON is a naval engineer at the Combat Direction Systems Activity (CDSA) Dam Neck, part of the Naval Surface Warfare System Dahlgren Division (NSWCDD) in Virginia Beach, Virginia. He earned his BS degree from Old Dominion University in Norfolk, Virginia (Mechanical Engineering, 2015). While at ODU, Mr. Johnson was an undergraduate research assistant engaged in Navy-funded research in areas of ship design requirements for directed-energy weapon integration, structural response modeling for high-performance vessels, as well as exploration of unmanned underwater glider technology. Mr. Johnson may be reached at bjohn087@odu.edu

JENNIFER GRIMSLEY MICHAELI, is an assistant professor of engineering technology at Old Dominion University and the director of the University's Naval Engineering and Marine Systems Institute (NEMSI). Dr. Michaeli earned her BS degree from Webb Institute of Glen Cove, New York (Naval Architecture and Marine Engineering, 1998), her MS degree from the Massachusetts Institute of Technology of Cambridge, Massachusetts (Ocean Systems Management, 1999), and her PhD from Old Dominion University (Mechanical Engineering). She is a licensed professional engineer in Virginia. At ODU, Dr. Michaeli is actively engaged in funded research for the Naval S&T community and in developing and promoting government-academia-industry partnerships to further the advancement of naval and marine engineering, and foster the future professional engineering workforce. Previously, she spent 15 years as a naval engineer and program manager both in the public and private sector of the naval enterprise and shipbuilding industries. In recognition for her contributions and accomplishments throughout her career, she is a recipient of the ASNE Young Engineer of the Year Award, the Navy's RADM Melville Award, ODU BCET Excellence in Research Award, and has twice been selected as ODU's nominee for the SCHEV Rising Star Award. Dr. Michaeli may be reached at jgmichae@odu.edu

ANALYSIS AND FEASIBILITY OF A HYBRID POWER SYSTEM FOR SMALL RURAL AREAS

Masoud Fathizadeh, Purdue University Northwest

Abstract

In many parts of the world, large cities enjoy power from a network or grid. However, remote villages do not have access to such technology. The purpose of this study was to analyze and assess the feasibility of electricity delivery to a village in a remote area. The author analyzed the feasibility of a hybrid power system for small rural areas. Several configurations of hybrid energy systems incorporating wind, solar, and battery storage were evaluated for being able to replace current stand-alone diesel power systems. Implementation of these configurations can result in the reduction of dependency on fuel and improved environmental footprints. Commercial software packages are available for simulation of hybrid electrical systems. One of the readily available simulation software packages was used to analyze the economic and environmental feasibility of a hybrid power system consisting of a wind turbine, solar panels, battery storage, and diesel generators. Where wind and solar availability is random and may not be accessible or able to support peak power demand, diesel generators can be utilized to accommodate for such situations.

Introduction

Electrification of rural locations in the past was promoted on the idea that reasonable access to electricity would improve the quality of living and, therefore, the economic well-being of the residents. However, rural electrification neither stopped the continued migration of rural individuals from the country to towns nor the decline of family farms. Electricity is a crucial pillar of world socioeconomic development and is the foremost requirement for technological advancement in production, heath, agriculture, and overall quality of normal life. In major industrial countries, access to electricity and its reliable availability was addressed long ago. However, various remote areas in developing countries do not seem to be connected to a centralized facility [1-2].

Grid connection of low population areas, particularly those located in hard to reach terrain, requires high capital expenditure with inherent high transmission losses. A study performed by the World Bank on rural electrification programs estimates the typical price of grid extension to be between $8000 and $10,000 per km and is expected to rise to around $22,000 per km in troublesome and hard to reach locations [3].

The dependability and reliability of the electrical grid is a crucial issue in delivering electrical power to remote areas. In order to collect data relating to the load, status of power delivery, and power sources, smart grid technology has been employed in recent years. A smart grid combines communications and power to collect data from the load and the overall system and optimally manages the power delivery [4, 5]. Application of a smart grid in remote rural areas is not a viable option, due to its cost and lack of access to an electrical grid. Diesel or gas generators are currently being used to supply electricity to these places, but supplying their fuel and considering their environmental issues makes their use somewhat undesirable. In this study, the author investigated the feasibility of rural electrification via alternative energy resources. This study was part of a grant to study the electrification of remote villages in different parts of the world. The selected location was intended to represent a typical village in the world with similar seasonal conditions. The selected village was located in a remote part of Indiana. The village was assumed to have a clinic, two schools, and street lighting as its public load. However, the clinic had to be powered continuously and, thus, was considered as a critical load. A factory constituted an industrial/commercial load, and family houses were considered residential loads. Based on the available data in this area, it was concluded that renewable resources in the village for generating electric power were

1. Solar energy
2. Wind turbine
3. Battery back-up

A diesel generator could be used if the above sources were not sufficient to support the loads during the peak demand. A simulation was performed to study the feasibility, cost, and performance of the system.

Simulation

Numerous products for modelling and simulation of renewable energy sources have been created and showcased lately. Nonetheless, the HOMER software programming

---

package gives the point-by-point details of ordered repro-duction and streamlining in a model that is moderately basic and simple to utilize. It is versatile and is applicable to a wide assortment of tasks. For a town or large-scale power framework, HOMER can demonstrate both the technical and financial components required in the evaluation. For bigger frameworks, HOMER can give a vital review that provides the expense and practicality of various setups, after which the user can utilize more specific programming to demonstrate specialized execution [6]. The project first runs an hourly simulation of every single conceivable design. The pace of handling the simulation takes into account the assessment of a large number of mixes. This hourly repro-duction additionally gives enhanced accuracy over measura-ble models that commonly assess average month-to-month execution of a framework. HOMER additionally models the halfway load effectiveness of diesel generators. This feature investigates the lower limit of a generator when it is not working at full load.

HOMER organizes the doable cases all together based on their net present (or lifecycle) values. The expense costs incorporate the value of part replacement, operation, up-keep, and fuel costs. HOMER records the ideal framework arrangement, characterized as the one with the minimum net present expense, for every framework considered. HOMER can provide sensitivity analysis on the critical parameters affecting the overall system performance. For example, fuel value or load sensitivity analysis can be performed to deter-mine their impact on system cost and performance [6]. The power plant in this project was made up of a wind turbine, photovoltaic arrays, converter, batteries, and a diesel gener-ator as a back-up during peak power demand. For simula-tion purposes, the annual average data for wind speed and solar radiation were used. The typical value for rural hybrid electrical system was given by Grégoire [7]. The minimum operating time for this system was 742 hours annually. This translates to a minimum of 2.5 days per month. This value is needed to define the lower limit for system performance. The input values used for minimum values of other parame-ters are shown in the following:

Wind turbine capacity = 225KW
Hub height = 40 meter
PV array capacity = 12.5 KW
Battery capacity = 16kWh/year
Diesel generator capacity = 220kVA =176 KW
Generator operational cost = $86/Hour
Cost of power from grid = $0.47/kWh
Cost of selling power to grid = $0.20/kWh
Average annual wind speed = 6.218m/s
Average annual clearness index = 0.500
Average annual solar radiation = 4.828 (kWh/m^2/d)
Diesel fuel price = $0.876/L

The following computer simulation was performed in order to assess the viability of the hybrid electrical system for the remote rural village.

Homer Simulation Configuration: In order to use the HOMER simulation software, a setup page had to be con-figured and proper values for parameters selected. The setup page for this project is shown in Figure 1.

Wind Turbine: The wind turbine was selected based on the available wind, the location, and the electrical load. In order to satisfy the above conditions, a 250 kW WES30 wind tur-bine was selected. The fixed cost for this turbine was $82,600 and the cost for operation and maintenance (O&M) was $1420/year. The wind turbine parameters shown in the setup page of Figure 1.
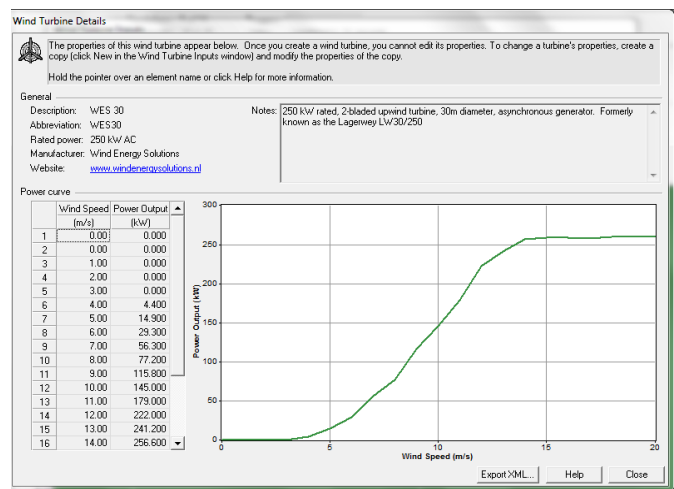
Figure 1. Simulation Setup Page

Diesel Generator: A 176 kW Perkins diesel generator was selected and the values for its parameters are given below:

Rating:	176 kW for continuous operation
Engine:	Perkins 6.6L in-line 6-cylinder diesel
Type:	turbocharged with direct injection
Cooling:	liquid
Generator:	brushless generator end (fan-cooled), +/-1% AC voltage regulation
Indicator:	low-oil and high-water temperature shutdown
Air filter:	high-volume air filter
Operation:	500-hour continuous
Battery:	12 V
Battery charger:	12 V alternators
Cold start:	glow plugs for cold weather starting
Frame:	welded steel skid base with rubber vi-bration mounts
Control Panel:	full w/ hour meter [8]

Figure 2 shows the setup page for the diesel generator.

Figure 2. Diesel Generator Setup Page

<u>PV Panel</u>: The photovoltaic source utilized for this project employed Solar Edge grid-tied system with combined panel -level power optimizers and monitoring with a specialized DC-AC string inverter to maximize the energy yield of a solar installation.

The maximum power point tracking (MPPT) on each panel mitigates partial string shading, panel mismatch, uneven soiling, and aging variance losses. The system was designed to automatically maintain a fixed-string voltage to ensure that the inverter always operates as efficiently as possible, regardless of string size, shading, or temperature. This allows flexible string length ranging from 8 to 25 panels and mitigates the performance impact of varying panel sizes, tilts, or orientations [9]. The PV system setup for HOMER is shown in Figure 3.

<u>Battery</u>: The batteries were selected to be reliable with long life [10]. The properties are as follows and the setup page is shown in Figure 4.

Life: 20 years
Battery type: 16OPZS2000
Amp-hour: 2217 @ 72 ºF

Simulation Results

Table 1 shows the system input parameters for simulation; Table 2 shows a summary of the costs. For the simulation, the average wind speed and diesel fuel costs are given as follows:

Wind data scaled average: 8 m/s
Diesel price: 0.8 $/L

Figure 3. Photovoltaic System Setup Page

**Figure 4. Battery Properties**

Table 1. System Architecture

PV array	12.5 kW
Wind turbine	1 WES 30
176 kW diesel	176 kW
Grid	100 kW
Inverter	25 kW
Rectifier	25 kW

Table 2. Cost Summary

Total net present cost	$ 528,534
Levelized cost of energy	$ 0.024/kWh
Operating cost	$ 19,205/yr

The grid cost is negative, meaning that electrical power can be supplied to the grid, while the cost for the diesel generator is positive with respect to its operation. Table 3 shows the capital, operating, and maintenance, as well as the total costs for PV, wind turbine, diesel generator, converters, and other parts of the system. It can be seen that more than $1.9 million can be saved utilizing the described hybrid electrical system. The fuel costs for the generator are substantial and represent major expenditures. Investment in PV and wind turbines as well as battery storage can substantially reduce dependency on the diesel generator. Table 4 shows the annualized cost for the different components of the system. The net savings for the PV was $3740 and $6462 for the wind turbine.

The impact of the savings results in a total system cost of $22,141 per year. Figure 5 shows the cash flow chart for the system. The bars on the positive side of the vertical axis show the savings on the electric bill not paid to the utility grid, while the bar on the negative side represents initial investment and operating costs. Table 5 shows a summary of power production from solar, wind, diesel, and network along with their percentage of contribution. The contribution of the PV array is very small (1%). Increasing the PV array size and battery system can offset the cost of operation of the diesel generator.
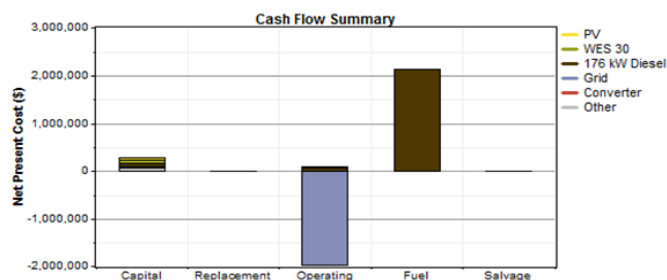
Figure 5. Cash Flow Summary

Table 3. Net Present Costs

Component	Capital	Replacement	O&M	Fuel	Salvage	Total
	($)	($)	($)	($)	($)	($)
PV	47,812	0	12,783	0	0	60,595
WES 30	82,600	0	18,152	0	0	100,752
176 kW Diesel	63,812	0	64,735	2,126,802	0	2,255,349
Grid	0	0	-1,978,253	0	0	-1,978,253
Converter	25,000	0	1,278	0	0	26,278
Other	63,812	0	0	0	0	63,812
System	283,036	0	-1,881,304	2,126,802	0	528,535

Table 4. Annualized Costs

Component	Capital	Replacement	O&M	Fuel	Salvage	Total
	($/yr)	($/yr)	($/yr)	($/yr)	($/yr)	($/yr)
PV	3,740	0	1,000	0	0	4,740
WES 30	6,462	0	1,420	0	0	7,882
176 kW Diesel	4,992	0	5,064	166,373	0	176,429
Grid	0	0	-154,752	0	0	-154,752
Converter	1,956	0	100	0	0	2,056
Other	4,992	0	0	0	0	4,992
System	22,141	0	-147,168	166,373	0	41,346

Table 5. Electrical Data

Component	Production	Fraction
	(kWh/yr)	
PV array	23,308	1%
Wind turbine	929,647	55%
176 kW Diesel	742,720	44%
Grid purchases	5,680	0%
Total	1,701,354	100%

Table 6 gives a summary of electricity consumption and sales to the grid. Table 7 gives electricity production from the PV array.

Table 6. Electrical Calculation

Load	Consumption	Fraction
	(kWh/yr)	
AC primary load	912,500	54%
Grid sales	785,357	46%
Total	1,697,857	100%

Table 7. Photovoltaic Array

Quantity	Value	Units
Rated capacity	12.5	kW
Mean output	2.66	kW
Mean output	63.9	kWh/d
Capacity factor	21.3	%
Total production	23,308	kWh/yr
Minimum output	0.00	kW
Maximum output	15.3	kW
PV penetration	2.55	%
Hours of operation	4,382	hr/yr
Levelized cost	0.203	$/kWh

Table 8 shows electricity production from the wind turbine. The turbine was rated at 250 kW and produced about 42% of its rated capacity. It operates 7998 hours per year compared to 8760 hours for full year. The cost of produced electricity per kWh from this unit was 0.8 cents and 20.3 cents for the PV units.

Table 8. AC Wind Turbine—WES 30

Variable	Value	Units
Total rated capacity	250	kW
Mean output	106	kW
Capacity factor	42.4	%
Total production	929,647	kWh/yr
Minimum output	0.00	kW
Maximum output	260	kW
Wind penetration	102	%
Hours of operation	7,998	hr/yr
Levelized cost	0.00848	$/kWh

Table 9 shows the operating output data for the diesel generator. The generator operates almost half of the year to compensate for the power from other units. It starts more than once a day (457 starts/year). The wind turbine generates more electricity than the diesel generator. This project only utilized one wind turbine. The load from the diesel generator can be substantially reduced if more than one wind turbine is installed.

Table 9. Diesel Generator Data

Quantity	Value	Units
Hours of operation	4,220	hr/yr
Number of starts	457	starts/yr
Operational life	0.176	yr
Capacity factor	48.2	%
Fixed generation cost	9.65	$/hr
Marginal generation cost	0.176	$/kWhyr
Electrical production	742,720	kWh/yr
Mean electrical output	176	kW
Min. electrical output	176	kW
Max. electrical output	176	kW
Fuel consumption	207,966	L/yr
Specific fuel consumption	0.280	L/kWh
Fuel energy input	2,046,384	kWh/yr
Mean electrical efficiency	36.3	%

Table 10 shows the data for the operation of the converter. The data reveal that only 9% of converter's capacity was utilized. This low percentage confirms the minimal utilization of the PV panels. The data for the grid for different months of the year is shown in Table 11. The energy sold to the utility company surpassed the purchased amount by a ratio of 250-to-1. In order to optimize the design, a smaller diesel generator and a larger wind turbine can be employed.

Table 10. Data for Converter

	Inverter	Rectifier	Units
Capacity	25.0	25.0	kW
Mean output	2.3	0.0	kW
Minimum output	0.0	0.0	kW
Maximum output	13.0	0.0	kW
Capacity factor	9.0	0.0	%
Hrs of operation	4,382	0.0	hrs/yr
Energy in	23,308	0.0	kWh/yr
Energy out	19,812	0.0	kWh/yr
Losses	3,496	0.0	kWh/yr

Table 12 demonstrates the significant reduction in two harmful gases, carbon dioxide (CO_2) and sulfur dioxide (SO_2), due to the application of the hybrid electrical system.

Table 12. Emissions

Pollutant	Emissions (kg/yr)
Carbon dioxide	-224,238
Carbon monoxide	1,352
Unburned Hydrocarbons	150
Particulate matter	102
Sulfur dioxide	-1,037
Nitrogen oxides	11,017

Analysis of Results

The viability of a hybrid electrical system for a remote village was investigated. This location was selected as it could be considered a typical village in a rural part of the Midwestern United States. It also provided insight into wind and solar energy utilization in this part of the country. The hybrid system employed a wind turbine, photovoltaic arrays, battery banks, diesel generator, and grid connections. The grid connection was added in the simulation to compare the produced electricity with the grid and potential for power trade and credit and net-metering. The minimum requirement for system operation was 742 hours, or 2.5 days per month. This value was selected as a minimum value in the simulation setup. The wind generator and PV array operated

Table 11. Grid Rate for Different Month of the Year

Month	Energy Purchased	Energy Sold	Net Purchases	Peak Demand	Energy Charge	Demand Charge
	(kWh)	(kWh)	(kWh)	(kW)	($)	($)
Jan	262	68,197	-67,935	20	0	99
Feb	283	61,572	-61,289	20	0	100
Mar	377	67,727	-67,350	19	0	93
Apr	327	68,183	-67,856	19	0	96
May	473	73,120	-72,648	20	0	100
Jun	620	70,743	-70,123	20	0	100
Jul	710	68,730	-68,020	20	0	99
Aug	692	66,562	-65,870	20	0	99
Sep	600	63,065	-62,465	20	0	100
Oct	462	55,866	-55,405	20	0	100
Nov	530	52,018	-51,488	20	0	99
Dec	344	69,573	-69,229	20	0	98

7998 and 4382 hours, respectively, which were far beyond the minimum of 742 hours. The simulation results revealed that majority of the load was carried by the wind turbine and diesel generator. An increase in the number of generators can substantially reduce the dependency on diesel fuel. The PV arrays contributed a small amount of electricity compared to the wind turbine. Investment should be focused on wind turbines rather than PV arrays in this part of the country. From the simulation in this study, it was found that the total capital cost for the system was \$283,360 and the total O&M was \$19,205. The net present cost (NPC) was \$528,534, which was the calculated profit for this project over 25 years. Economically, then, the system is very feasible. The reduction in harmful emissions such as SO_2 and CO_2 makes this project environmentally attractive as well.

Conclusion

A study was performed to analyze the viability of hybrid energy and storage technology for a remote village. The study confirmed previous results obtained for hybrid systems in rural communities in developing countries worldwide. In locations where abundant wind and solar resources are available, the configurations of hybrid energy systems incorporating wind energy, solar energy, and battery storage can be successful. The study confirmed the feasibility of these hybrid systems with many configurations being profitable. Another attribute of the hybrid system was its improved environmental aspects and minimized CO_2 emissions and cost of operation. The simulation also revealed the following:

a. The data analysis for the wind turbine showed that very low or no wind speeds have a large negative impact on the output power of the wind turbine and the hybrid system compared to the positive impact of high winds.

b. An increase in the demand for electricity requires an increase in diesel generator usage. Under this condition, an increase in diesel fuel prices can result in a substantial increase in both the net present cost of the system and the CO_2 emissions.

c. Cloudy days have adverse effects on PV power production and increased usage of the diesel generator.

d. The battery system is sufficient to carry essential loads under emergency conditions.

References

[1] Rehman, S., Ahmad, F., Shaahid, S. M., Shash, A., El-Amin, I. M., Al-Shehri, A. M., et al. (2011). Feasibility Study of Hybrid Retrofits to an Isolated Off-Grid Diesel Power Plant. *Renewable and Sustainable Energy Reviews, 11*, 635-653. http://dx.doi.org/10.1016/j.rser.2005.05.003

[2] Mackay, D. (2009). *Sustainable Energy—Without the Hot Air*. Cambridge: UIT Cambridge Ltd.

[3] Moner-Girona, M. (2008). A New Scheme for the Promotion of Renewable Energies in Developing Countries: The Renewable Energy Regulated Purchase Tariff. Retrieved from http://www.energy.eu/publications/LDNA23284ENC_002.pd

[4] Huber P., & Mills M. (2005). *The Bottomless Well*. New York: Basic Books.

[5] Wind Energy: The Facts (2013). Analytical Methods for the Prediction of the Long-Term Wind Regime at a Site. Retrieved from http://www.wind-energy-the-facts.org/analytical-methods-for-he-prediction-of-the-long-term-wind-regime-at-a-site.html

[6] HOMER Energy (2013). Optimizing Clean Power Everywhere. Energy Modeling Software for Hybrid Renewable Energy Systems. Retrieved from http://homerenergy.com/index.htm

[7] Grégoire L., (2013). Rural Electrification with PV Hybrid Systems, Overview and Recommendations for Further Deployment (IED). Retrieved from https://www.iea.org/media/openbulletin/Rural_Electrification_with_PV_Hybrid_systems.pd, ISBN 978-3-906042-11-4

[8] Perkins Corporation. Retrieved from www.perkins.co

[9] Blue Pacific Solar Corporation. Retrieved from http://www.bluepacificsolar.com/home-solar/solaredge-12500w-solar-kit.htm

[10] Hoppecke Battery Inc. Retrieved from http://www.hoppecke-us.com/

Biographies

MASOUD FATHIZADEH is an associate professor of electrical and mechatronic engineering technology at Purdue University Northwest. He earned his BS in Electrical Engineering from the University of Science and Technology Tehran, Iran; MS in Electrical Engineering from the University of Toledo; and, Doctor of Engineering in Electrical Engineering from Cleveland State University. Dr. Fathizadeh is currently teaching at Purdue University Northwest. His interests include electrical power, control, energy, and renewable energy sources. Dr. Fathizadeh may be reached at fathizad@pnwl.edu

INSTRUCTIONS FOR AUTHORS:
MANUSCRIPT SUBMISSION REQUIREMENTS

The INTERNATIONAL JOURNAL OF ENGINEERING RESEARCH AND INNOVATION is an online/print publication. Articles appearing in IJERI generally focus on engineering-related research but also may branch out to diverse fields related to technological innovation and entrepreneurship. All submissions to this journal, including manuscripts, peer-reviews of submitted documents, requests for editing changes, as well as notification of acceptance or rejection, will be handled electronically.

All manuscript submissions must be prepared in Microsoft Word (.doc or .docx) and contain all figures, images, and/or pictures embedded where you want them and appropriately captioned. It is highly recommended that you print, in color, all images in your manuscript in order to determine their quality; the journal editors will be doing the same during the editorial review of your manuscript. If your manuscript is accepted for publication, you will receive instructions regarding all required revisions and the submission of higher-quality images. If you are able to provide such images, it's possible that you will be asked to remove them from the manuscript.

Tables must be created directly in Word, not imported as pictures, and be enclosed on all sides. If you have graphs or charts, they should also be created directly in Word, if possible. If that is not possible, the editor will discuss further options with you. Please be conscientious of the quality of your images and remember that all online and print copies of issues of IJERI are in color.

The editorial staff of the International Journal of Engineering Research and Innovation reserves the right to format and edit any submitted document in order to meet publication standards of the journal. Included here is a summary of the formatting instructions. You should, however, review the "sample Word document" included on our website (http://ijeri.org/formatting-guidelines) for a detailed analysis of how to correctly format your manuscript.

The references included in the References section of your manuscript must follow APA-formatting guidelines. In order to help you, the sample Word document also includes numerous examples of how to format a variety of sources. If you have a reference source for which you are not able to find the correct APA format, contact me for help anytime (philipw@bgsu.edu). Keep in mind that an incorrectly formatted manuscript will be returned to you, a delay that may cause it to be moved to a subsequent issue of the journal.

1. Word document page setup: Top = 1", Bottom = 1", Left = 1.25", Right = 1.25". This is the default setting for Microsoft Word.

2. Page breaks, tabs, and indents: Do not use page breaks or tabs. Do not use spaces for paragraph indents; use the scroll markers, as shown here.

3. Paper title: Centered at the top of the first page with a 22-point Times New Roman (Bold), Small-Caps font.

4. Body fonts: Use 10-point Times New Roman (TNR) for body text throughout (1/8" paragraph indention); 9-point TNR for author names/affiliations under the paper title; 16-point TNR for major section titles; 14-point TNR for minor section titles; 9-point TNR BOLD for caption titles; other font sizes may be noted in the sample Word document.

5. Images: All images should be included in the body of the document. It's ok for images or tables to be centered on the page, and not confined to the 2-column format, if necessary. Irrespective of how Word moves any given image/table, be certain that all captions are located in the document where the images/tables should ultimately be placed. If you are required to submit additional high-quality images, they must be saved/sent as individual files (one image per file) and labeled using the following format, where the first portion of the title is your manuscript number:
J16-F-09 Figure 7

6. In-text referencing: List and number each reference when referring to them in the body of the document (e.g., [1]). In-text references must be in numerical order and follow entries in the References section. Again, see the sample Word document on our website for specifics. Please do not use the End-Page Reference utility in Microsoft Word.

7. Tables and figures: Captions for tables must be above the table, while captions for figures are below; all captions are left-justified unless the table or figure is centered on the page, in which case the caption should also be centered.

8. Page limit: Manuscripts should not be more than 15 pages (single-spaced, 2-column format).

9. Page numbering: Do not use page numbers.
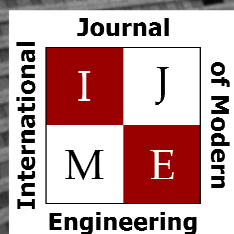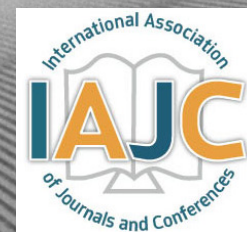
INTERNATIONAL JOURNAL OF
MODERN ENGINEERING

ABOUT IJME:

- IJME was established in 2000 and is the first and official flagship journal of the International Association of Journal and Conferences (IAJC).

- IJME is a high-quality, independent journal steered by a distinguished board of directors and supported by an international review board representing many well-known universities, colleges and corporations in the U.S. and abroad.

- IJME has an impact factor of **3.00**, placing it among the top 100 engineering journals worldwide, and is the #1 visited engineering journal website (according to the National Science Digital Library).

OTHER IAJC JOURNALS:

- The International Journal of Engineering Research and Innovation (IJERI)
  For more information visit www.ijeri.org

- The Technology Interface International Journal (TIIJ).
  For more information visit www.tiij.org

IJME SUBMISSIONS:

- Manuscripts should be sent electronically to the manuscript editor, Dr. Philip Weinsier, at philipw@bgsu.edu.

  For submission guidelines visit www.ijme.us/submissions

TO JOIN THE REVIEW BOARD:

- Contact the chair of the International Review Board, Dr. Philip Weinsier, at philipw@bgsu.edu.

  For more information visit www.ijme.us/ijme_editorial.htm

INDEXING ORGANIZATIONS:

- IJME is indexed by numerous agencies. For a complete listing, please visit us at www.ijme.us.

Contact us:

Mark Rajai, Ph.D.

Editor-in-Chief
California State University-Northridge
College of Engineering and Computer Science
Room: JD 4510
Northridge, CA 91330
Office: (818) 677-5003
Email: mrajai@csun.edu

TIIJ International

www.tiij.org

IJERI International Journal of Engineering Research & Innovation
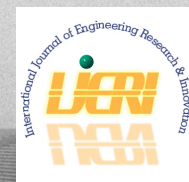
www.ijeri.org

IJERI

The International Journal of Engineering Research & Innovation (IJERI) is the second official journal of the International Association of Journals and Conferences (IAJC). IJERI is a highly-selective, peer-reviewed print journal which publishes top-level work from all areas of engineering research, innovation and entrepreneurship.